Structural Analysis of Helios Filament-Wound Tanks Subjected to Internal Pressure and Cooling

William L. Ko
NASA Dryden Flight Research Center
Edwards, California

January 2005

The NASA STI Program Office…in Profile

Since its founding, NASA has been dedicated to the advancement of aeronautics and space science. The NASA Scientific and Technical Information (STI) Program Office plays a key part in helping NASA maintain this important role.

The NASA STI Program Office is operated by Langley Research Center, the lead center for NASA's scientific and technical information. The NASA STI Program Office provides access to the NASA STI Database, the largest collection of aeronautical and space science STI in the world. The Program Office is also NASA's institutional mechanism for disseminating the results of its research and development activities. These results are published by NASA in the NASA STI Report Series, which includes the following report types:

- TECHNICAL PUBLICATION. Reports of completed research or a major significant phase of research that present the results of NASA programs and include extensive data or theoretical analysis. Includes compilations of significant scientific and technical data and information deemed to be of continuing reference value. NASA's counterpart of peer-reviewed formal professional papers but has less stringent limitations on manuscript length and extent of graphic presentations.

- TECHNICAL MEMORANDUM. Scientific and technical findings that are preliminary or of specialized interest, e.g., quick release reports, working papers, and bibliographies that contain minimal annotation. Does not contain extensive analysis.

- CONTRACTOR REPORT. Scientific and technical findings by NASA-sponsored contractors and grantees.

- CONFERENCE PUBLICATION. Collected papers from scientific and technical conferences, symposia, seminars, or other meetings sponsored or cosponsored by NASA.

- SPECIAL PUBLICATION. Scientific, technical, or historical information from NASA programs, projects, and missions, often concerned with subjects having substantial public interest.

- TECHNICAL TRANSLATION. English-language translations of foreign scientific and technical material pertinent to NASA's mission.

Specialized services that complement the STI Program Office's diverse offerings include creating custom thesauri, building customized databases, organizing and publishing research results…even providing videos.

For more information about the NASA STI Program Office, see the following:

- Access the NASA STI Program Home Page at *http://www.sti.nasa.gov*

- E-mail your question via the Internet to help@sti.nasa.gov

- Fax your question to the NASA STI Help Desk at (301) 621-0134

- Telephone the NASA STI Help Desk at (301) 621-0390

- Write to:
  NASA STI Help Desk
  NASA Center for AeroSpace Information
  7121 Standard Drive
  Hanover, MD 21076-1320
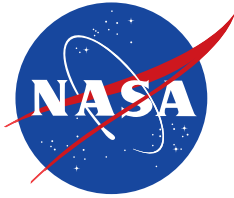
NASA/TM-2005-212855

Structural Analysis of Helios Filament-Wound Tanks Subjected to Internal Pressure and Cooling

William L. Ko
NASA Dryden Flight Research Center
Edwards, California

January 2005

Cover art: NASA Dryden Flight Research Center, photograph ED01-0209-5.

Available from:

CONTENTS

ABSTRACT

A finite-element stress analysis is performed on Helios filament-wound hydrogen tanks to examine the stress field and effect of end dome geometry on the stress field. Each tank is composed of a central circular cylindrical section with either geodesic or hemispherical end domes, which have metallic polar bosses. The tanks are subjected to combined and separate internal pressure and temperature loading conditions, and the stress contributions of each loading component are examined. The tank-wall–polar-boss interfacial meridional tensile stress in the hemispherical dome is found to be approximately 27 percent lower than that in the geodesic dome. The effects of both material anisotropy and the aluminum lining on the intensities of tensile meridional stress at the tank-wall–polar-boss bonding interface are examined.

NOMENCLATURE

a	radius of tank circular cylindrical section, in.
Al	aluminum
b	outer radius of polar boss, in.
c	length of polar boss, in.
d	depth of tank end dome, in.
E	modulus of elasticity, lb/in^2
E_θ	hoop (θ) modulus of elasticity, lb/in^2
E_ϕ	meridional (ϕ) modulus of elasticity, lb/in^2
l	length of tank circular cylindrical section, in.
N_θ	hoop panel load, lb/in.
N_ϕ	meridional panel load, lb/in.
p	internal pressure, lb/in^2
r, z	cylindrical coordinates
t_b	thickness of polar boss wall, in.
t_s	thickness of tank wall, in.
T	temperature, ˚F
α	coefficient of thermal expansion, in/in ˚F
α_θ	hoop coefficient of thermal expansion, in/in ˚F
α_ϕ	meridional coefficient of thermal expansion, in/in ˚F
β	helix angle, measured from the generatrix of cylinder, deg
δ_r	tank wall radial displacement (in cylindrical coordinate system), in.
δ_z	tank wall axial displacement in z-direction, in.
v	Poisson's ratio
$v_{\phi\theta}, v_{\theta\phi}$	Poisson's ratio associated with meridional (ϕ) and hoop (θ) directions
ρ	density, lb/in^3
σ_θ	hoop stress, lb/in^2
σ_ϕ	meridional stress, lb/in^2

INTRODUCTION

The Helios prototype unmanned aerial vehicle (UAV), pictured on the cover of this report, is a solar-powered, ultralightweight, high-altitude (to 100,000 ft), long duration flying wing. During the day the aircraft is powered by solar energy, and at night it is to be powered by a unique fuel cell system. This system requires lightweight tanks containing both the hydrogen and oxygen constituents of the fuel cell. Through the use of an electrolyzer, excess electrical energy, generated by the solar cells during the day, is used to disassociate water molecules. The resulting oxygen and hydrogen gases are then accumulated in separate tanks. At night, when the solar cells stop producing electricity, the process is reversed. The oxygen and hydrogen gases are fed into the fuel cell, which produces electricity, water, and heat. The electricity is used to power the Helios until the following morning when the solar cells take over and the power cycle starts all over again. If this concept is successfully demonstrated, Helios flights could last for several months and could induce a new generation of long duration aircraft called atmospheric satellites.

Because the hydrogen tank volume is 2.25 times larger than the oxygen tank volume, weight is a critical factor for the Helios. The tanks required for both hydrogen and oxygen storage, therefore, must be as light as possible. Filament-wound pressure vessels, which are as much as 50 percent lighter than comparable all-metal tanks, have been proposed for use as the hydrogen and oxygen gas storage tanks (refs. 1–9).

During operation, each Helios filament-wound tank (a short cylindrical section with geodesic end domes) will be subjected to internal pressure and high-altitude cooling. As a result, the tank wall will be subjected to a biaxial tensile stress field. At the boundary of the circular cylindrical polar boss, the tension-carrying fibers cannot follow the diameter of the polar boss; they can be only tangent to the outer surface of the polar boss. Therefore, tension-carrying filaments carry the hoop stress at the boss boundary, and the interfacial meridional tensile stress (which becomes radial at the polar opening) is carried by the matrix. Because the matrix has relatively low tensile strength, the polar boss geometry must be designed to reduce the interfacial meridional tensile stress. One design approach is to develop a flanged polar boss and lap bond it to the wall of the filament-wound tank, which would transfer a portion of the meridional tensile stress into shear stress. This approach could eliminate potential leakage or bursting near the tank-wall–polar-boss bonding region. This approach was used in the preliminary design of scale model tanks. During the proof tests, however, a gas leakage occurred at the polar boss and composite bonding region, resulting in a tank burst initiated at the polar boss region. Therefore, a thorough understanding of the structural behavior of filament-wound pressure vessels with polar boss openings is crucial.

A finite-element stress analysis has been performed on proposed Helios filament-wound hydrogen tanks to examine the stress field and effect of end dome geometry on the stress field, particularly at the tank-wall–polar-boss bonding interface. Hydrogen tanks are larger and more critical than oxygen tanks. This report provides basic information concerning the structural behavior of Helios filament-wound hydrogen tanks with geodesic or hemispherical end domes.

FILAMENT-WOUND PRESSURE VESSELS

Because of high tensile strength in the fiber direction, thin filaments are good candidates for the fabrication of high strength and lightweight pressure vessels. For example, the ultimate tensile strength of

T-1000 carbon filaments can exceed 1,000,000 lb/in^2 (refs. 1, 2). To fully benefit from the ultrahigh unidirectional strength of the filaments, however, winding the filaments in the direction of the maximum principal stress is essential. This task is accomplished by winding the filaments on a mandrel in such a manner that the angle of the wrap (helix angle, measured from the meridian) is in the direction of the maximum stress. During the winding of the filaments, uniform tension is applied and the filaments are impregnated with resin. After curing, the filaments and resin will develop sufficient shear strength to attain the high tensile strength of the fibers in the form of a composite structure. After the mandrel is removed, the resulting composite shell structure will have an exceptional strength-to-weight ratio, as much as 50 percent lighter than a comparable all-metal tank (refs. 1–9).

In addition to providing a structure of high strength-to-weight ratio, this manufacturing procedure offers other advantages. For example, the shell connection can be eliminated, and the cylindrical section, end closures, skirt, and so forth, can be fabricated as a single unit. These integral end closures allow the precise design of pressure cylinders of various proportions over a wide range of sizes and loading conditions.

In closed-end cylindrical pressure vessels, the ratio of hoop stress to longitudinal stress acting in the wall is 2 to 1, but in spherical vessels, the ratio of hoop stress to meridional stress acting in the wall is 1 to 1 (equal-biaxial or isotropic stress field). Thus, in metal pressure vessel design, the spherical vessel is more advantageous than the cylindrical vessel because of the isotropic stress field. In the design of metallic cylindrical vessels, the cylindrical wall thickness must be able to withstand the hoop stress even though the longitudinal stress is only one-half of the hoop stress. Because metals are essentially isotropic in strength, the product of operating pressure and volume capacity for each unit weight of material is less for a cylindrical vessel than for a spherical vessel for a given peak stress.

When the remarkably high unidirectional tensile strength of the filaments is used, designing a filament-wound pressure vessel to attain maximum performance efficiency is possible. For this purpose, three basic filament winding systems usually are used: longitudinal, circumferential, and helical. A helix is a geodesic of a cylindrical surface, which will turn into a straight line if the cylinder is unfolded into a plane. Longitudinal and circumferential winding systems provide only unidirectional reinforcement. The helical winding system can provide biaxial reinforcement of the vessel. For example, in filament-wound cylinders, the filament reinforcement can be oriented and proportioned so that the hoop strength of the cylinder wall is actually twice the longitudinal strength. This orientation is accomplished by winding the filaments at the optimal helical winding angle ($\beta = \tan^{-1} \sqrt{2} = 54.7356$ deg) measured from the generatrix (a straight line parallel to the longitudinal axis) of the cylindrical surface (refs. 10, 11).

During the winding of an integral end dome closure for a cylindrical pressure vessel, the so-called isotensoid dome shape is quite popular. This dome geometry is mathematically determined and looks like a modified oblate spheroid (a surface formed by the rotation of an ellipse about its minor axis). When winding over the isotensoid domed vessel under the optimal helical winding angle, the filaments will trace a geodesic of the curved surface, and every filament, regardless of its location in the structure, is subjected to the same constant tensile stress (isotensoid) (refs. 12, 13). The geodesic is a curve of minimum length joining a pair of points on a given curvilinear surface. The geodesics of the cylindrical and spherical surfaces are the helix and great circle (the geodesic of a sphere), respectively.

Another type of mathematically determined dome geometry is the so-called planar-wound dome (refs. 12, 13), over which the winding filaments lie in the same plane. This type of dome will resist internal

pressure loads without contributions from the resin; however, it is not isotensoid and is not examined in this report. During the winding of a spherical pressure vessel, because of the isotropic stress field, the so-called circumpolar (or great circle) system can be used to cause each filament to essentially describe a perfect hoop around the sphere (ref. 9).

FINITE-ELEMENT ANALYSIS

The structural performance and resizing (SPAR) program (ref. 14) was used in the finite-element analysis of the hydrogen tanks. The analysis examines the stress fields induced in the hydrogen tanks, structural deformations, and the intensities of the tensile meridional stress (debonding stress) induced at the tank-wall–polar-boss bonding interface, which is the most critical region.

Geometry

Helios hydrogen tanks (figs. 1 and 2) are filament-wound structures without metal lining. Tank dimensions are indicated in the figures. Each tank is composed of a central circular cylindrical section with either geodesic (fig. 1) or hemispherical (fig. 2) end domes. The poles of the domes have circular polar openings to which metallic polar bosses are bonded for the transfer of hydrogen gas.

Cases Analyzed

Two types of tank geometry were analyzed. Tank type 1, a Helios hydrogen tank with geodesic end domes, is an oblate spheroid, which has a surface formed by the rotation of an ellipse about its minor axis (fig. 1). Tank type 2 is a Helios tank with hemispherical end domes (fig. 2). In this analysis, the multilayered filament-wound tank wall was treated as one of the following:

1. Quasi-isotropic tank, in which both the cylindrical section and end domes have quasi-isotropic walls.

2. Hoop-reinforced tank, in which the hoop strength of the cylindrical section is doubled (that is, $E_\theta = 2E_\phi$), and the end domes have quasi-isotropic walls.

3. Quasi-isotropic tank with lining, in which 0.014-inch-thick aluminum lining is added to the quasi-isotropic tank (case 1).

Note that the meridional (longitudinal) and hoop stress ($\sigma_\phi = pa/2t_s$, $\sigma_\theta = pa/t_s$) induced in the cylindrical wall section are independent of material properties. The hoop reinforcement in case 2, however, affects the tank wall radial displacement in the cylindrical section.

Finite-Element Modeling

Because of symmetry, only one-quarter of a tank was modeled. Figures 3 and 4 show the finite-element models of the Helios hydrogen tanks with geodesic and hemispherical domes, respectively. These plots were generated from the one-quarter tank models, and the respective mirror images were added to form the half-tank plots. The tank and polar boss walls were modeled with a single layer of quadrilateral combined membrane and bending elements (E43 elements). The plug at the inner or outer

end of the polar boss was modeled with a single layer of triangular combined membrane and bending elements (E33 elements). Table 1 lists the size of each one-quarter tank model.

Table 1. Size of each one-quarter tank finite-element model.

Item	Number
JLOC	933
E43 elements	930
E33 elements	30

Materials

The polar boss material was either aluminum or stainless steel, which has a lower coefficient of thermal expansion than aluminum has. Table 2 lists the material properties for input to the finite-element models.

Table 2. Material properties.

	Composite walls (quasi-isotropic)[*]	Polar boss (aluminum)	Polar boss (stainless steel)[†]
$E(= E_\phi = E_\theta)$, lb/in^2	17.42×10^6	10.5×10^6	29.00×10^6
$v(= v_{\phi\theta} = v_{\theta\phi})$	0.038	0.23	0.276
ρ, lb/in^3	0.05984	0.101	0.282
$\alpha = (\alpha_\phi = \alpha_\theta)$, in/in ˚F	0.75×10^{-6}	12.5×10^{-6}	5.75×10^{-6}

* Carbon fiber composites.
[†] 17-7 PH stainless steel.

Loading

The tanks were subjected to three loading conditions: (1) combined pressure and temperature loading (referred to as "$p + T$" loading), (2) pressure loading only (referred to as "p-only" loading), and (3) temperature loading only (referred to as "T-only" loading), in which the internal pressure, p, was 400 lb/in^2, and the temperature, T, was –120 ˚F, simulating high-altitude cooling.

The interiors of the polar bosses were either pressure free ($p = 0$, with the polar boss inner end sealed) or pressurized (with the polar boss outer end sealed and the inner end open to a tank internal pressure of $p = 400$ lb/in^2).

RESULTS

This section discusses the results of the finite-element stress analysis of the Helios hydrogen tanks. Note that all figures present the data for the cases in which aluminum polar bosses were used.

Quasi-Isotropic Tanks

Figures 5–10 show the resulting deformed shapes of the two Helios hydrogen tank types with quasi-isotropic walls (and no lining) subjected to the three loading conditions ($p + T$, p-only, and T-only). Each figure shows the magnitude of radial displacement of the cylindrical wall (normal to the z-axis), δ_r, and the axial displacement of the polar boss (in the z-direction), δ_z. In all plots of the radial and axial displacement distributions (δ_r, δ_z), each arrow drawn normal to the tank wall contour indicates the magnitude of δ_r and δ_z only, and should not be confused with the actual direction of δ_r or δ_z. Notice that in the $p + T$ and p-only loading cases (figs. 5–8), the radial displacement, δ_r, suddenly increases at the cylinder-dome junctures, reflecting increases in the hoop stress, σ_θ, at the same regions.

In the geodesic dome tank under $p + T$ loading (fig. 5) the radial displacement, δ_r, is slightly negative. It is negative because the radial displacement, δ_r, at the cylinder-dome juncture under p-only loading (fig. 7) is very small (two order of magnitude smaller than δ_r at the cylindrical section) and cannot overcome the inward radial displacement, δ_r, resulting from T-only loading (fig. 9). This peculiar structural behavior (that is, negligible radial displacement at the cylinder-dome juncture) occurs because the geodesic dome, under internal pressure, tends to deform into a hemispherical shape, and the bending effect tends to constrain the juncture to move outward, resulting in very small δ_r at the juncture. This structural behavior is examined in the Appendix through the use of an isolated geodesic dome subjected to p-only loading. In the hemispherical dome tank (figs. 6, 8, 10), this peculiar structural behavior at the cylinder-dome juncture does not occur. In the T-only loading cases (figs. 9,10), the dome polar region bends inward because of the shrinkage of the metallic polar bosses.

Figures 11 and 12 show the meridional distributions of tank wall axial displacement, δ_z, for the two types of dome geometry. The polar region axial displacement, δ_z, of the hemispherical dome is roughly 50 percent that of the geodesic dome under the $p + T$ and p-only loading conditions.

The effect of T-only loading (the difference between the $p + T$ and p-only loading curves) causes the axial displacement of the polar boss to be less than that of the surrounding wall ($p + T$ loading curves), which is why the tank wall appears to slightly bulge in the region surrounding the polar boss (figs. 5, 6). The effect of T-only loading on δ_z is very small except in the polar boss region.

Figures 13 and 14 show the meridional distributions of radial displacement, δ_r, for the two types of dome geometry. In the geodesic dome case (fig. 13), the radial displacement, δ_r, sharply decreases and becomes slightly negative at the cylinder-dome juncture. In the hemispherical dome case (fig. 14), the value of δ_r decreases to one-half at the cylinder-dome juncture.

6

Table 3 lists the displacement of the quasi-isotropic tank wall at critical points for the two types of dome geometry. Two sets of data are listed; the upper rows indicate the cases in which the polar bosses were not pressurized, and the lower rows (shown in parentheses) indicate the cases in which the polar bosses were pressurized ($p = 400$ lb/in^2). Note that the effects of the polar boss material and internal pressure on the tank wall displacement are minuscule.

Table 3. Quasi-isotropic tank wall displacement at the cylindrical section, δ_r, and polar boss, δ_z.

Dome type	Polar boss material	Loading condition	δ_r, in. (cylindrical section)	δ_z, in. (polar boss)
Geodesic	Al	p-only	0.117 (0.117)	0.158 (0.158)
		T-only	-0.289×10^{-2}	-0.286×10^{-1}
		$p + T$	0.114 (0.114)	0.129 (0.130)
	Steel	$p + T$	0.114 (0.114)	0.143 (0.144)
Hemispherical	Al	p-only	0.117 (0.117)	0.0862 (0.0868)
		T-only	-0.289×10^{-2}	-0.263×10^{-1}
		$p + T$	0.114 (0.114)	0.0599 (0.0605)
	Steel	$p + T$	0.114 (0.114)	0.0721 (0.0727)

( ) $p = 400$ lb/in^2 applied inside the polar bosses.

Figures 15 and 16 show the meridional distributions of meridional stress, σ_ϕ, for the two types of dome geometry. For the geodesic dome (fig. 15), the value of σ_ϕ is constant in the cylindrical zone and gradually increases towards the polar boss region. For the hemispherical dome (fig. 16), σ_ϕ is constant everywhere except for the small region near the polar boss. The T-only loading tends to increase the values of σ_ϕ at the tank-wall–polar-boss interface (see the $p + T$ curves in figs. 15 and 16).

Figures 17 and 18 show the meridional distributions of hoop stress, σ_θ, for the two types of dome geometry. For the geodesic dome (fig. 17), the value of σ_θ is constant in the cylindrical zone, decreases rapidly to nearly zero at the cylinder-dome juncture, then increases towards the polar boss region, and finally decreases slightly at the polar boss. For the hemispherical dome (fig. 18), σ_θ decreases to one-half at the cylinder-dome juncture, and remains constant in the dome region except at the polar boss. The T-only loading considerably decreases the values of σ_θ at the tank-wall–polar-boss interface (see the $p + T$ curves in figs. 17 and 18).

Table 4 lists the stress induced at the polar boss locations in the quasi-isotropic tank walls under various loading conditions. The upper rows of data indicate the cases in which the interiors of the polar bosses were not pressurized, and the lower rows of data (shown in parentheses) indicate the cases in which the polar bosses were pressurized ($p = 400$ lb/in^2).

Table 4. Stress at the tank-wall–polar-boss interface for quasi-isotropic tanks.

Dome type	Polar boss material	Loading condition	σ_ϕ, lb/in^2	σ_θ, lb/in^2
Geodesic	Al	p-only	73,000 (72,920)	64,120 (64,410)
		T-only	4,210	−13,580
		$p + T$	77,210 77,120	50,530 (50,860)
	Steel	$p + T$	74,860 (74,710)	58,280 (58,650)
Hemispherical	Al	p-only	52,700 (52,600)	46,330 (46,740)
		T-only	3,380	−13,240
		$p + T$	56,070 (55,970)	33,090 (33,530)
	Steel	$p + T$	54,130 (54,030)	40,700 (41,120)

( ) $p = 400$ lb/in^2 applied inside the polar bosses.

Note that the meridional and hoop stress of the hemispherical dome type are 27 and 35 percent lower, respectively, than that of the geodesic dome type. Also note that changing the polar boss material from aluminum to steel (thus lowering the coefficient of thermal expansion) and applying pressure inside the polar boss cavity have very little effect on reducing the tank-wall–polar-boss interfacial meridional tensile stress.

Hoop-Reinforced Tanks

Figures 19–24 show the deformed shapes of two types of hoop-reinforced tanks under various loading conditions. The radial displacement in the cylindrical sections decreases to approximately one-half of that in the quasi-isotropic tank. The geodesic dome type still exhibits the stepwise change of radial displacement, δ_r, at the cylinder-dome juncture under the $p + T$ and p-only loading conditions (figs. 19 and 21, respectively). In the hemispherical dome case, however, the stepwise change of radial displacement, δ_r, completely disappears under the $p + T$ and p-only loading conditions (figs. 20 and 22, respectively).

Figures 25 and 26 show the meridional distributions of tank wall axial displacement, δ_z, for the two types of dome geometry. The δ_r profiles are very similar to those of the quasi-isotropic tanks (figs. 11, 12) except at the regions near the polar bosses.

Figures 27 and 28 show the meridional distributions of tank wall radial displacement, δ_r, for the two types of dome geometry. The value of δ_r in the cylindrical regions for the two cases is reduced nearly one-half because of the hoop reinforcement (see figs. 13 and 14).

Table 5 shows the tank wall displacement data for the two types of dome geometry when the hoop strength of the cylindrical section was doubled. The data for the quasi-isotropic tanks (from table 3) are shown in parentheses for comparison. Note that the differences between the two material types are relatively small.

Table 5. Hoop-reinforced tank wall displacement at the cylindrical section and polar boss, δ_z.

Dome type	Loading condition	δ_r, in. (cylindrical section)	δ_z, in. (polar boss)
Geodesic	p-only	0.0576 (0.117)	0.175 (0.158)
	T-only	-0.289×10^{-2} (-0.289×10^{-2})	-0.268×10^{-1} (-0.286×10^{-1})
	$p + T$	0.0547 (0.114)	0.148 (0.129)
Hemispherical	p-only	0.0576 (0.117)	0.0967 (0.0862)
	T-only	-0.289×10^{-2} (-0.289×10^{-2})	-0.249×10^{-1} (-0.263×10^{-1})
	$p + T$	0.0547 (0.114)	0.0718 (0.0599)

( ) Data for the quasi-isotropic tanks (from table 3).

The meridional distributions of meridional (figs. 29, 30) and hoop stress (figs. 31, 32) of the hoop-reinforced tanks are very similar to those of the quasi-isotropic tanks (figs. 15–18) except at the cylinder-dome junctures and the polar boss regions.

Table 6 lists the data for the interfacial stress at the tank-wall–polar-boss bonding surfaces in the two types of hoop-reinforced tanks. The data for the quasi-isotropic tanks (from table 4) are shown in parentheses for comparison. Note that in the $p + T$ loading case, the interfacial meridional stress, σ_ϕ, decreases by merely 4 percent, and the hoop stress, σ_θ, increases by roughly 25 percent, for both types of dome geometry when the hoop strength is doubled (figs. 31, 32).

Table 6. Stress at the tank-wall–polar-boss interface in hoop-reinforced tanks.

Dome type	Loading condition	σ_ϕ, lb/in^2	σ_θ, lb/in^2
Geodesic	p-only	73,520 (73,000)	75,830 (64,120)
	T-only	970 (4,210)	–13,220 (–13,580)
	$p + T$	74,490 (77,210)	62,610 (50,530)
Hemispherical	p-only	53,180 (52,700)	54,290 (46,330)
	T-only	600 (3,380)	–12,990 (–13,240)
	$p + T$	53,780 (56,070)	41,300 (33,090)

( ) Data for the quasi-isotropic tanks (from table 4).

Quasi-Isotropic Tanks with Aluminum Lining

The deformed shapes of the quasi-isotropic tanks with 0.014-inch-thick aluminum lining are quite similar to the deformed shapes of the tanks without lining (figs. 5–10). Figures depicting the deformed shapes of these tanks, therefore, are not presented.

Table 7 compares the displacement data for the aluminum-lined quasi-isotropic tanks to the corresponding displacement data for the tanks without lining (from table 3, shown in parentheses). Note that the wall displacement of the aluminum-lined tanks decreases slightly compared to the wall displacement of the corresponding quasi-isotropic tanks with no aluminum lining (table 3).

Table 7. Wall displacements of aluminum-lined quasi-isotropic tanks at the cylindrical section, δ_r, and polar boss, δ_z.

Dome type	Loading condition	δ_r, in. (cylindrical section)	δ_z, in. (polar boss)
Geodesic	p-only	0.105 (0.117)	0.134 (0.158)
	T-only	-0.288×10^{-2} (-0.289×10^{-2})	-0.352×10^{-1} (-0.286×10^{-1})
	$p + T$	0.102 (0.114)	0.0984 (0.129)
Hemispherical	p-only	0.105 (0.117)	0.0721 (0.0862)
	T-only	-0.286×10^{-2} (-0.289×10^{-2})	-0.311×10^{-1} (-0.263×10^{-1})
	$p + T$	0.102 (0.114)	0.041 (0.0599)

( ) Data for the quasi-isotropic tanks with no aluminum lining (from table 3).

Table 8 lists the stress induced at the tank-wall–polar-boss interface in the aluminum-lined tanks under various loading conditions. The stress in the composite wall and aluminum lining are shown to compare the stress sharing. Corresponding data for the quasi-isotropic tanks without lining (from table 4) are shown in parentheses.

Under $p + T$ loading, the aluminum lining reduces the level of tank-wall–polar-boss interfacial meridional stress, σ_ϕ, by only 10 and 17 percent for the geodesic and hemispherical dome types, respectively. Table 9 lists the interfacial panel loads (N_ϕ, N_θ; stress x thickness) at the tank-wall–polar-boss interface calculated from table 8. Under $p + T$ loading, the panel load shares for the aluminum lining are 10 and 11 percent for N_ϕ and N_θ, respectively, for both dome types.

11

Table 8. Stress at the tank-wall–polar-boss interface in aluminum-lined quasi-isotropic tanks.

Dome type	Loading condition	σ_ϕ, lb/in^2		σ_θ, lb/in^2	
		Tank wall	Al lining	Tank wall	Al lining
Geodesic	*p*-only	65,160 (73,000)	45,900	53,960 (64,120)	39,000
	T-only	4,170 (4,210)	−5,200	−13,060 (−13,580)	−13,070
	p + *T*	69,330 (77,210)	40,700	40,900 (50,530)	25,930
Hemispherical	*p*-only	43,940 (52,700)	31,840	39,290 (46,330)	28,490
	T-only	2,500 (3,380)	−5,000	−12,420 (−13,240)	−12,220
	p + *T*	46,440 (56,070)	26,840	26,870 (33,090)	16,270

( ) Data for the quasi-isotropic tanks with no aluminum lining (from table 4).

Table 9. Interfacial panel loads (N_ϕ, N_θ) at the tank-wall–polar-boss interface in aluminum-lined quasi-isotropic tanks.

Dome type	Loading condition	N_ϕ, lb/in.		N_θ, lb/in.	
		Tank wall	Al lining	Tank wall	Al lining
Geodesic	*p*-only	5,148	643	4,263	546
	T-only	329	−73	−1,032	−183
	p + *T*	5,477	570	3,231	363
Hemispherical	*p*-only	3,471	446	3,103	399
	T-only	198	−70	−981	−171
	p + *T*	3,669	376	2,122	228

CONCLUDING REMARKS

A finite-element stress analysis was performed on Helios filament-wound hydrogen tanks with two types of end domes. Tank deformations, stress fields, and intensities of the tensile meridional stress (debonding stress) induced at the tank-wall–polar-boss bonding interface were examined. The principal findings are as follows:

1. The wall around the polar boss deformed with an apparent "dimple" in both the geodesic and hemispherical dome tanks because of the shrinking effect of the metallic end bosses.

2. Under pressure loading only and combined pressure and temperature loading, the inward axial displacement, δ_z, of the hemispherical dome tank end boss was roughly one-half that of the geodesic dome tank end boss.

3. For both the geodesic and hemispherical dome tanks, the radial displacement, δ_r, of the tank wall was much larger in the cylindrical wall region because of greater hoop stress, σ_θ.

4. The stress field in the geodesic dome was nonequal biaxial ($\sigma_\theta \neq \sigma_\phi$). The stress field in the hemispherical dome, however, was equal biaxial ($\sigma_\theta = \sigma_\phi$) everywhere, except at the tank-wall–polar-boss interface region.

5. The meridional stress, σ_ϕ, in the geodesic dome tank increased slightly along the meridian towards the polar boss, and then increased considerably as the tank-wall–polar-boss interface was approached. In the hemispherical dome tank, however, the meridional stress, σ_ϕ, was constant along the meridian, except at the tank-wall–polar-boss bonding interface region.

6. The hoop stress, σ_θ, in the geodesic dome tank reached infinitesimal value at the cylinder-dome juncture because of extremely small hoop expansion at the juncture site. In the hemispherical dome tank, however, the meridional distribution of hoop stress, σ_θ, did not have any "dented" regions.

7. The interfacial tensile meridional stress, σ_ϕ, at the tank-wall–polar-boss interface of the geodesic dome tank was approximately 27 percent greater than that of the hemispherical dome tank in both the quasi-isotropic and hoop-reinforced cases.

8. Doubling the hoop strength reduced the radial displacement but did not reduce the hoop stress in both the geodesic and hemispherical dome tanks.

9. When the end boss material was changed from aluminum to stainless steel, which has a lower coefficient of thermal expansion, the interfacial meridional tensile stress, σ_ϕ, decreased by only 3 percent in both dome types. Furthermore, varying the end boss material did not have much effect on reducing the interfacial tensile stress at the tank-wall–polar-boss interface.

10. The meridional and hoop load shares by the 0.014-inch-thick aluminum lining were approximately 10 and 11 percent for the geodesic and hemispherical dome tanks, respectively.
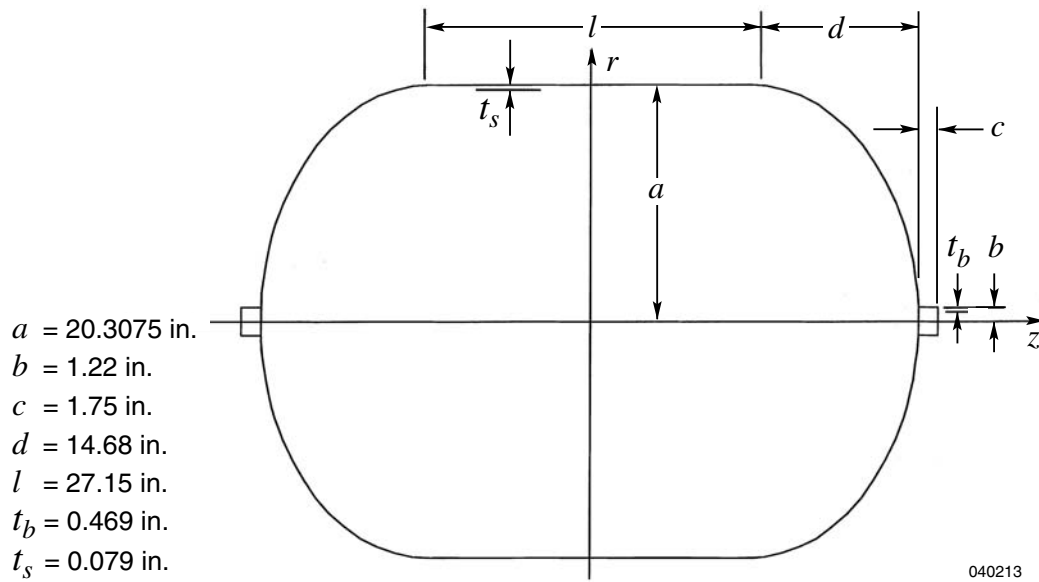
a = 20.3075 in.
b = 1.22 in.
c = 1.75 in.
d = 14.68 in.
l = 27.15 in.
t_b = 0.469 in.
t_s = 0.079 in.

040213

Figure 1. Geometry of Helios hydrogen tank with geodesic domes.

a = 20.3075 in.
b = 1.22 in.
c = 1.75 in.
d = *a*
l = 27.15 in.
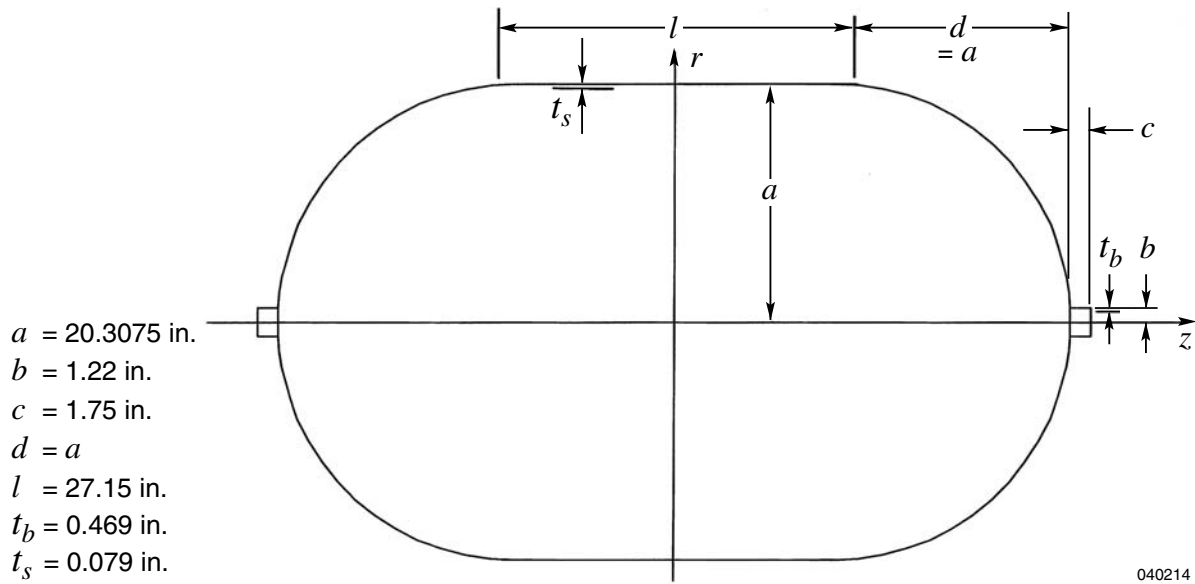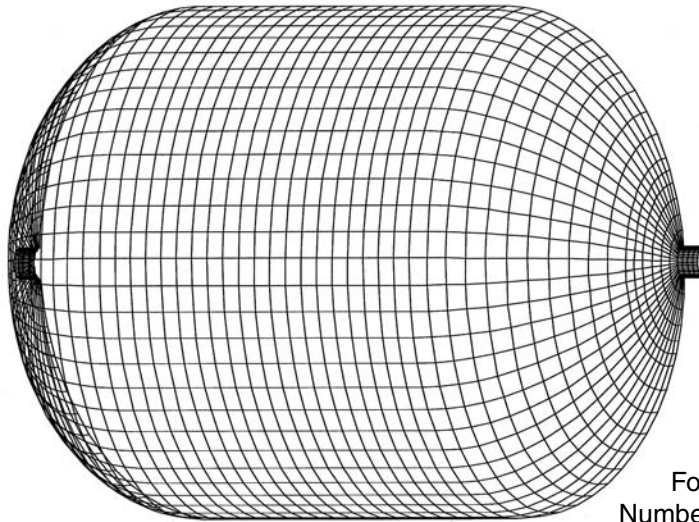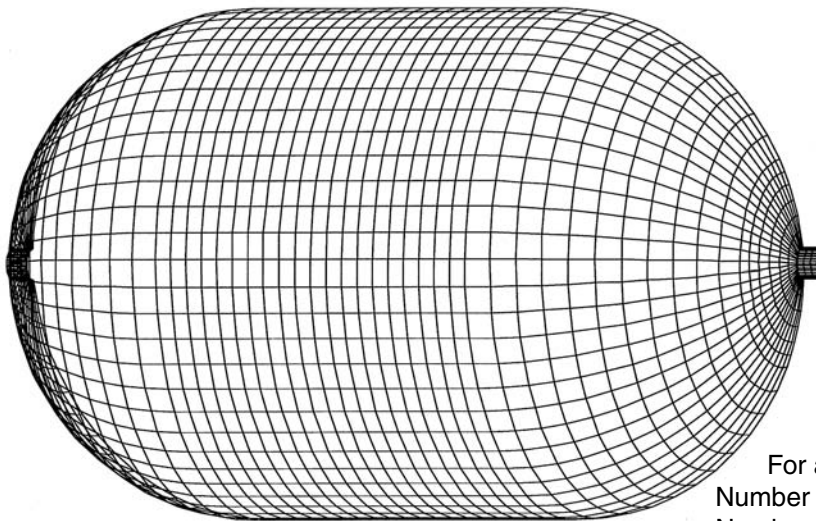t_b = 0.469 in.
t_s = 0.079 in.

040214

Figure 2. Geometry of generic Helios hydrogen tank with hemispherical domes.

For a one-quarter model
Number of nodes   993
Number of 4-node elements   930
Number of 3-node elements   30

040215

Figure 3. One-quarter tank finite-element model of the Helios geodesic dome tank (mirror image added to show one-half of the tank).

For a one-quarter model
Number of nodes   993
Number of 4-node elements   930
Number of 3-node elements   30

040216

Figure 4. One-quarter tank finite-element model of the Helios hemispherical dome tank (mirror image added to show one-half of the tank).

15

$\delta_r = 0.114$ in.

$\delta_r = -0.154 \times 10^{-2}$ in.

Deformed

Undeformed

$\delta_z = 0.129$ in.

$p + T$

040217
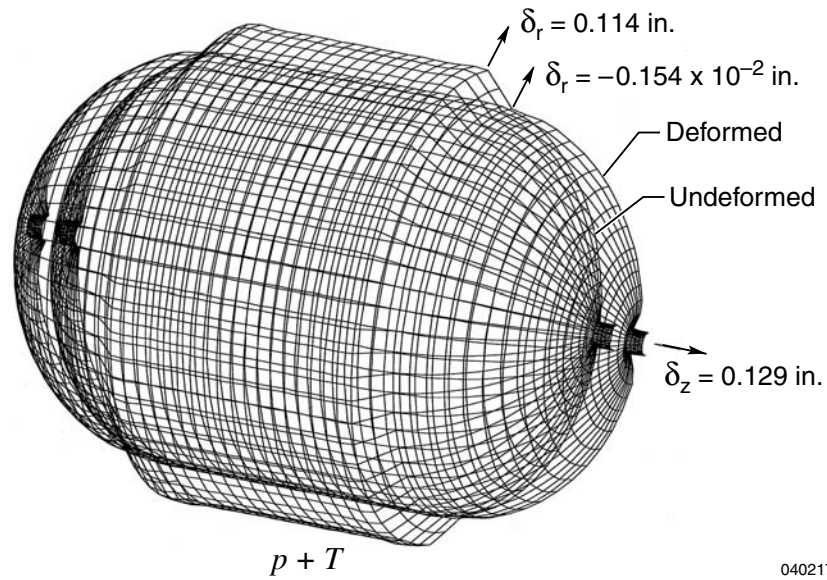
Figure 5. Deformed shape of Helios geodesic dome tank under internal pressure and temperature loading; $p = 400$ lb/in^2; $T = -120$ °F.

$\delta_r = 0.114$ in.

$\delta_r = 0.495 \times 10^{-1}$ in.

Deformed

Undeformed

$\delta_z = 0.599 \times 10^{-1}$ in.

$p + T$

040218
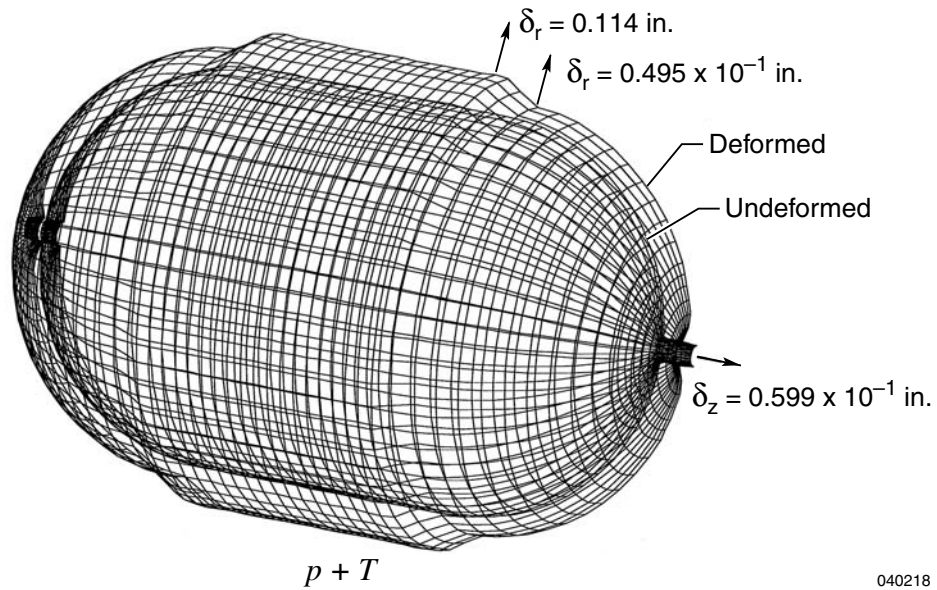
Figure 6. Deformed shape of Helios hemispherical dome tank under internal pressure and temperature loading; $p = 400$ lb/in^2; $T = -120$ °F.

16

$\delta_r = 0.117$ in.

$\delta_r = 0.134 \times 10^{-2}$ in.

Deformed

Undeformed

$\delta_z = 0.158$ in.

p-only

040219
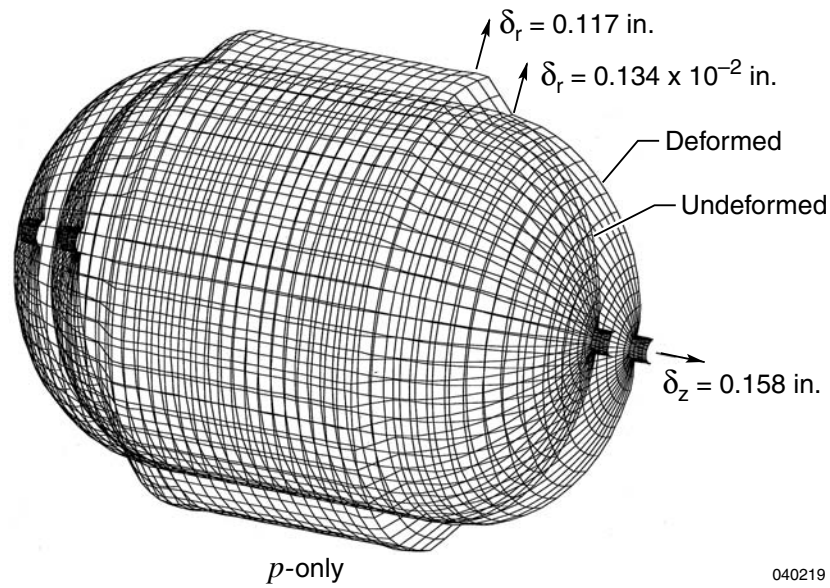
Figure 7. Deformed shape of Helios geodesic dome tank under internal pressure loading only; $p = 400$ lb/in^2.

$\delta_r = 0.117$ in.

$\delta_r = 0.524 \times 10^{-1}$ in.

Deformed

Undeformed

$\delta_z = 0.862 \times 10^{-1}$ in.

p-only

040220
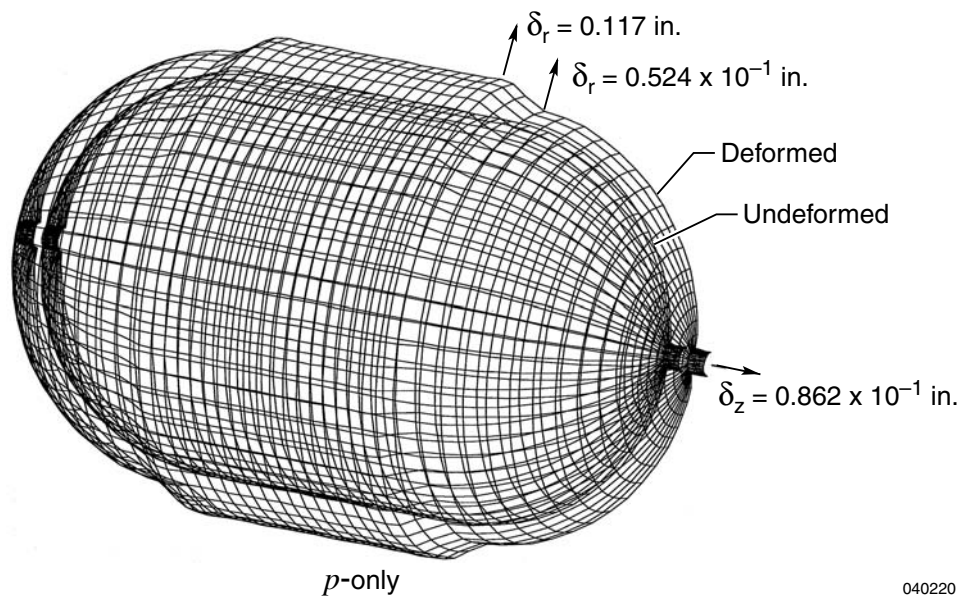
Figure 8. Deformed shape of Helios hemispherical dome tank under internal pressure loading only; $p = 400$ lb/in^2.

17

$\delta_r = -0.289 \times 10^{-2}$ in.

$\delta_r = -0.288 \times 10^{-2}$ in.

Deformed

Undeformed

$\delta_z = -0.286 \times 10^{-1}$ in.

T-only

040221
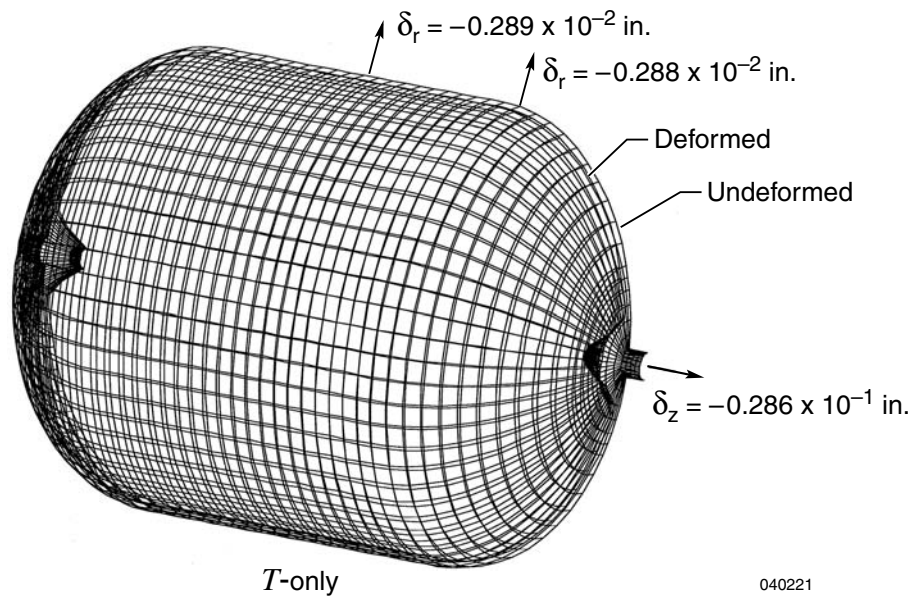
Figure 9. Deformed shape of Helios geodesic dome tank under temperature loading only; $T = -120$ °F.

$\delta_r = -0.289 \times 10^{-2}$ in.

$\delta_r = -0.288 \times 10^{-2}$ in.

Deformed

Undeformed

$\delta_z = -0.263 \times 10^{-1}$ in.

T-only

040222
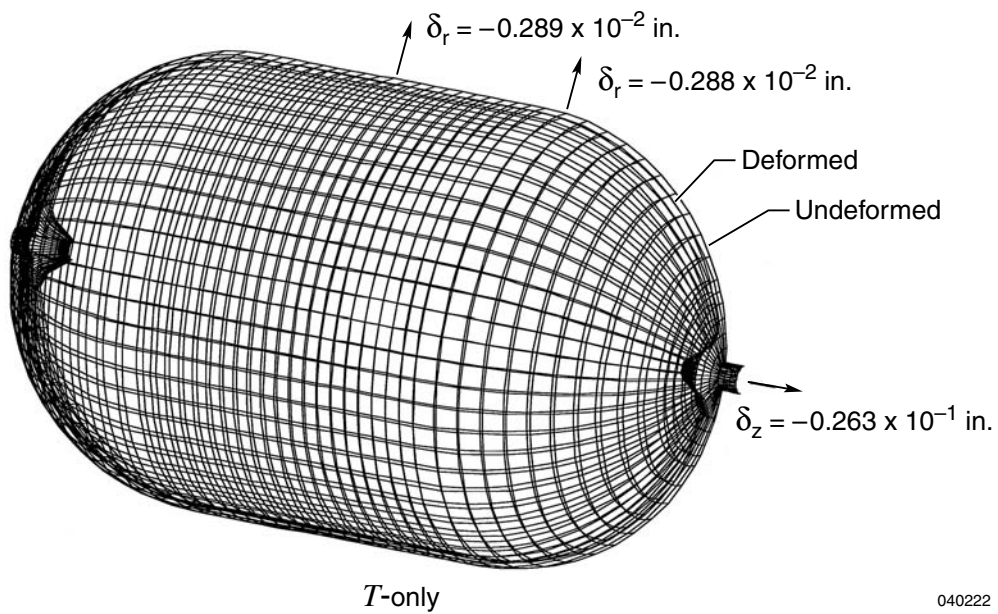
Figure 10. Deformed shape of Helios hemispherical dome tank under temperature loading only; $T = -120$ °F.

18
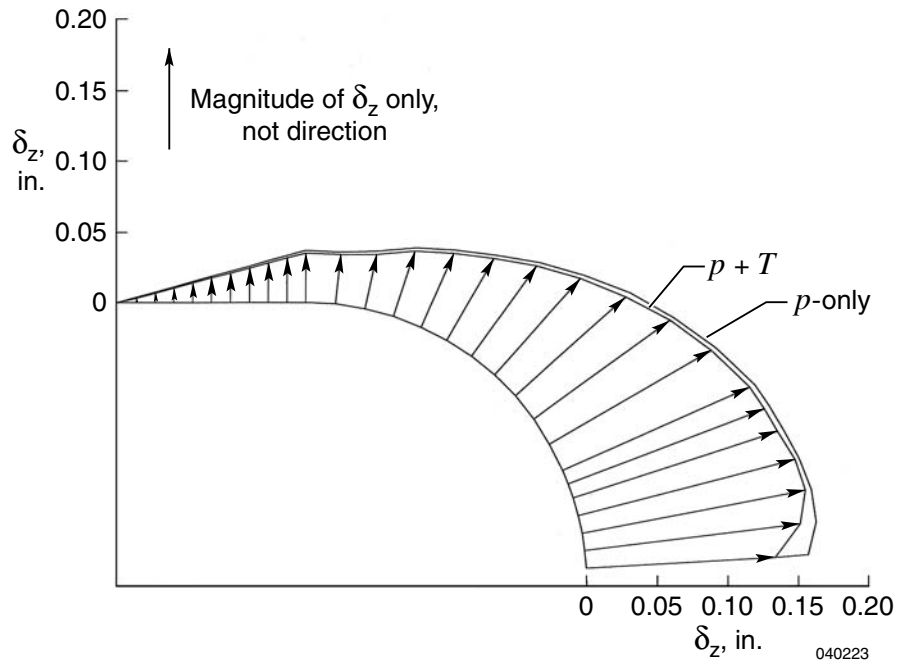
Figure 11. Meridional distributions of axial displacement, δ_z, of Helios geodesic dome tank wall; $p = 400$ lb/in^2; $T = -120$ °F.
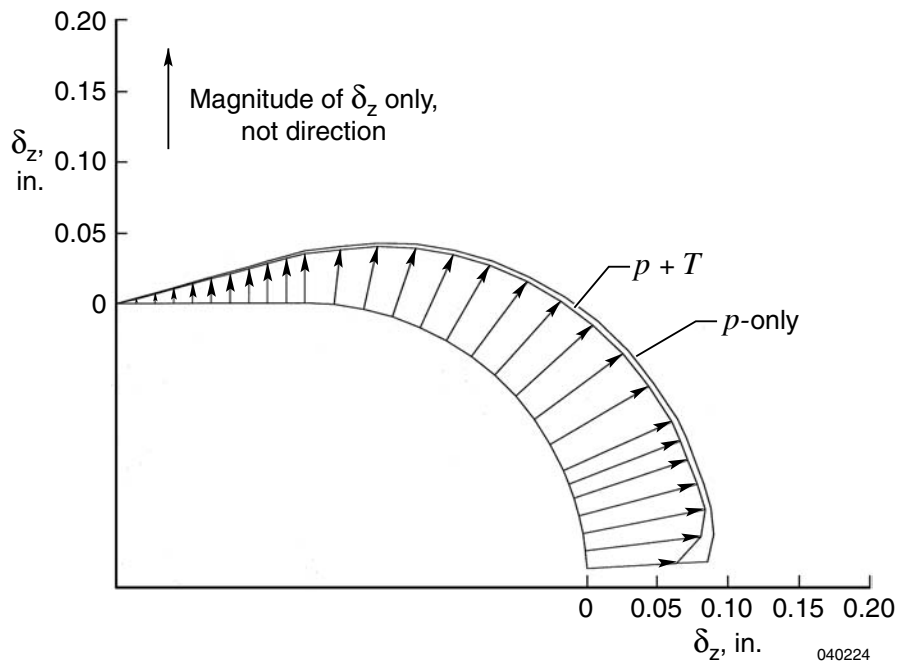
Figure 12. Meridional distributions of axial displacement δ_z of Helios hemispherical dome tank wall; $p = 400$ lb/in^2; $T = -120$ °F.

19
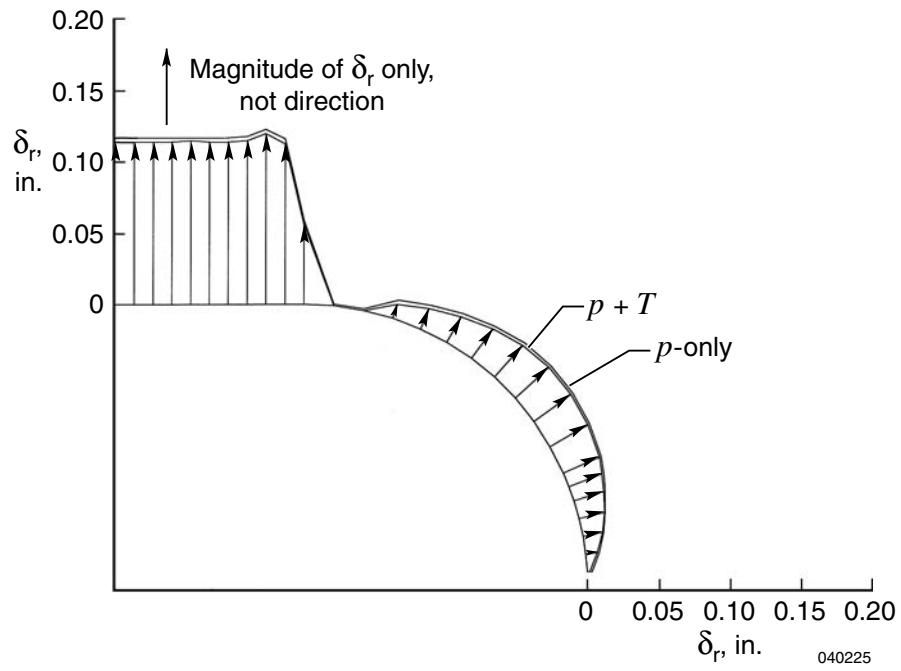
Figure 13. Meridional distributions of radial displacement, δ_r, of Helios geodesic dome tank wall; $p = 400$ lb/in^2; $T = -120$ °F.
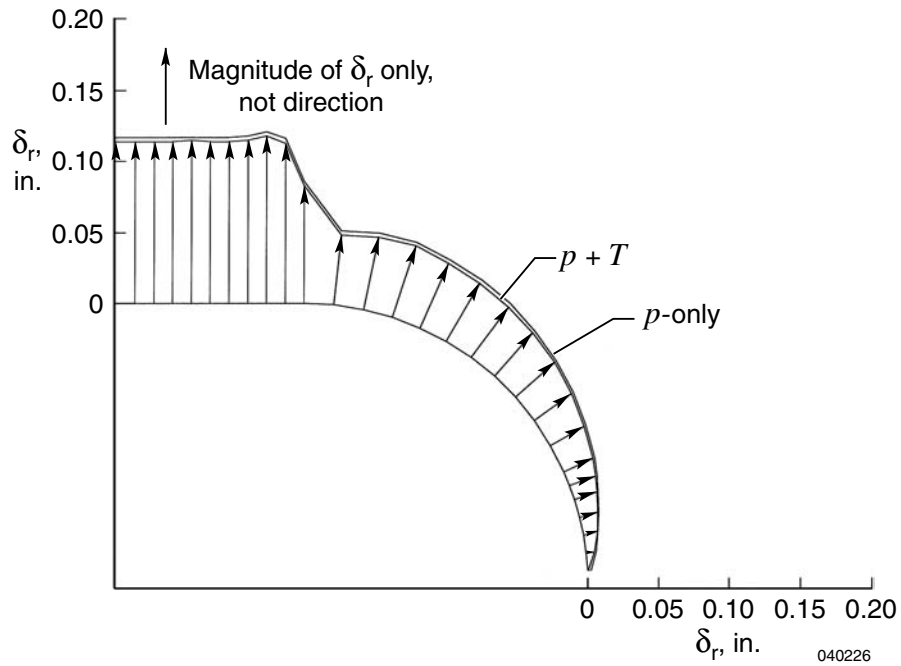
Figure 14. Meridional distributions of radial displacement, δ_r, of Helios hemispherical dome tank wall; $p = 400$ lb/in^2; $T = -120$ °F.
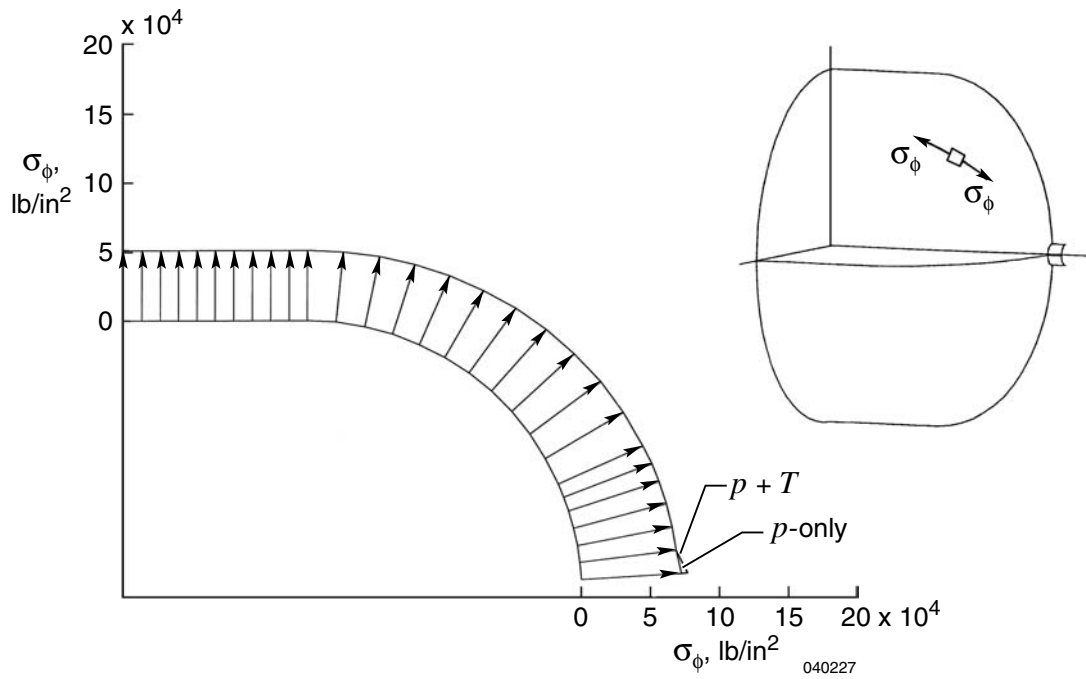
Figure 15. Meridional distributions of meridional stress, σ_ϕ, in Helios geodesic dome tank; $p = 400$ lb/in^2; $T = -120$ °F.
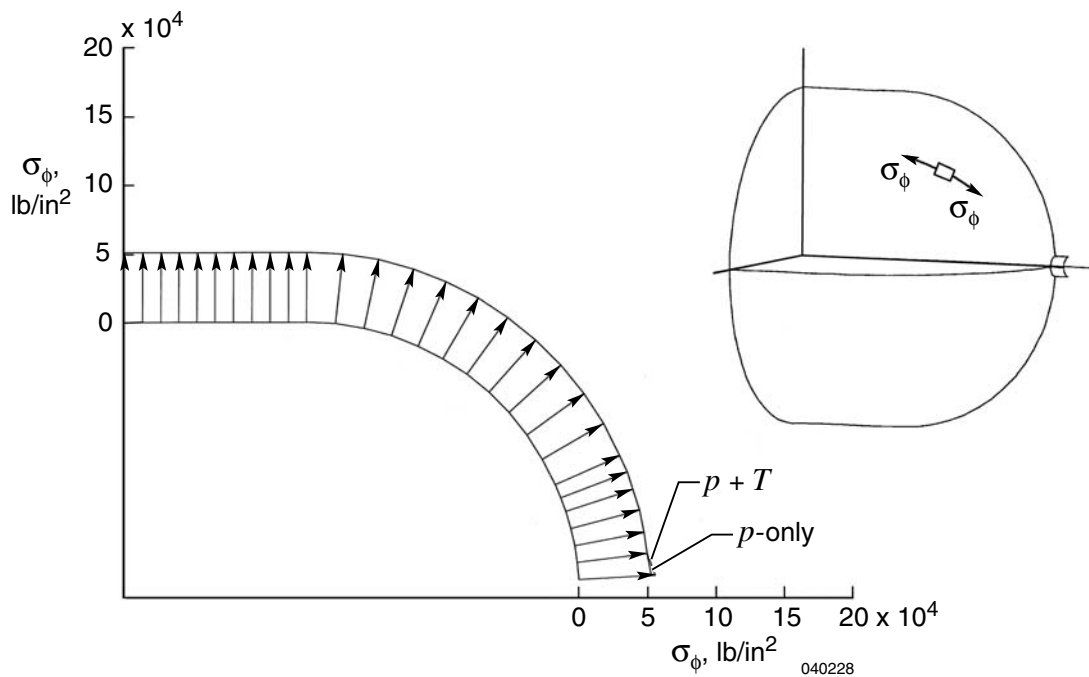
Figure 16. Meridional distributions of meridional stress, σ_ϕ, in Helios hemispherical dome tank; $p = 400$ lb/in^2; $T = -120$ °F.

21
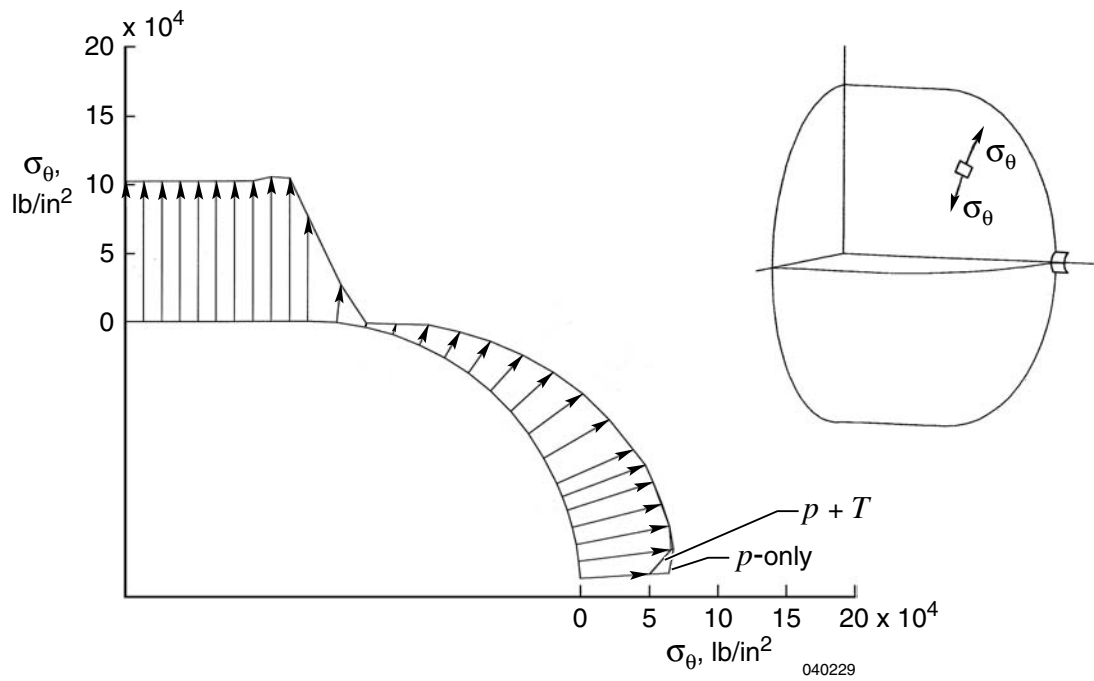
Figure 17. Meridional distributions of hoop stress, σ_θ, in Helios geodesic dome tank; $p = 400$ lb/in^2; $T = -120$ °F.
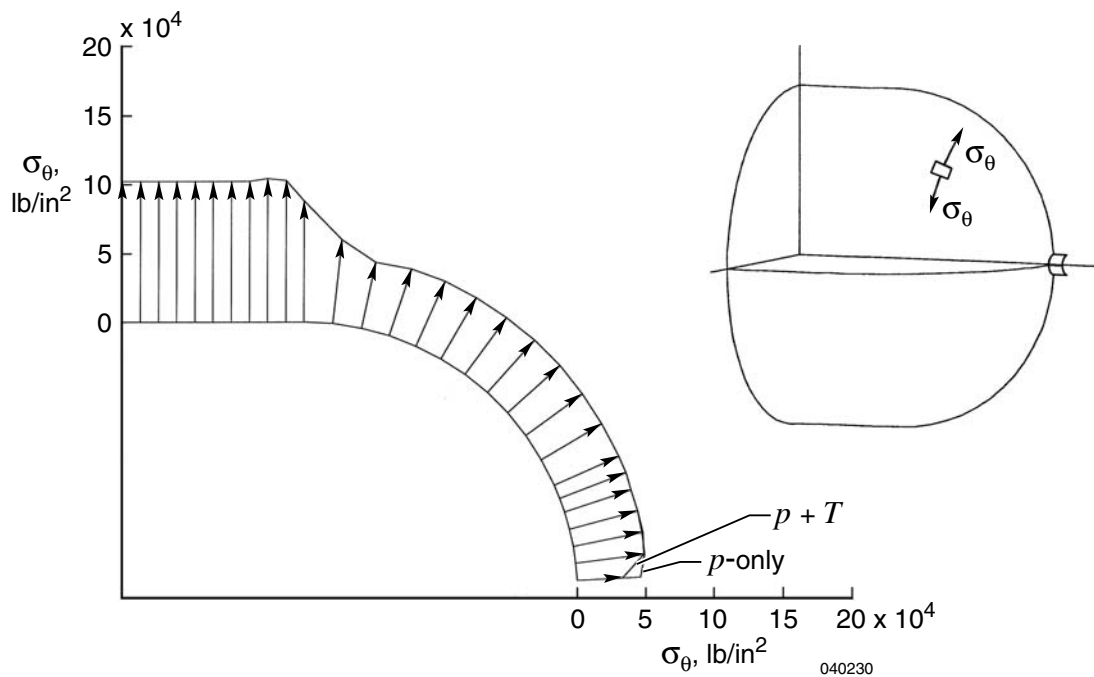
Figure 18. Meridional distributions of hoop stress, σ_θ, in Helios hemispherical dome tank; $p = 400$ lb/in^2; $T = -120$ °F.

$\delta_r = 0.547 \times 10^{-1}$ in.

$\delta_r = -0.414 \times 10^{-3}$ in.

Deformed

Undeformed

$\delta_z = 0.148$ in.

$p + T$

040231
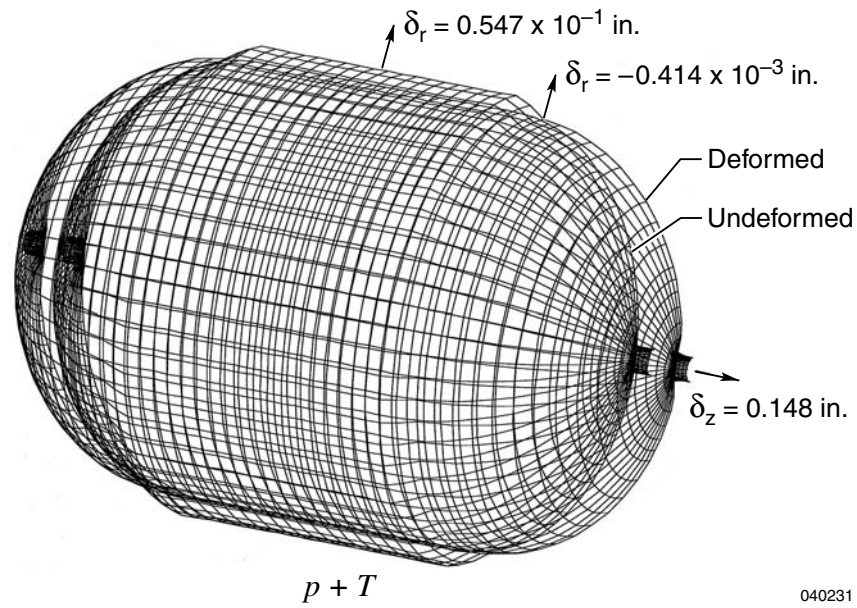
Figure 19. Deformed shape of Helios geodesic dome tank under internal pressure and temperature loading; $p = 400$ lb/in^2; $T = -120$ °F; hoop-reinforced cylindrical wall.

$\delta_r = 0.547 \times 10^{-1}$ in.
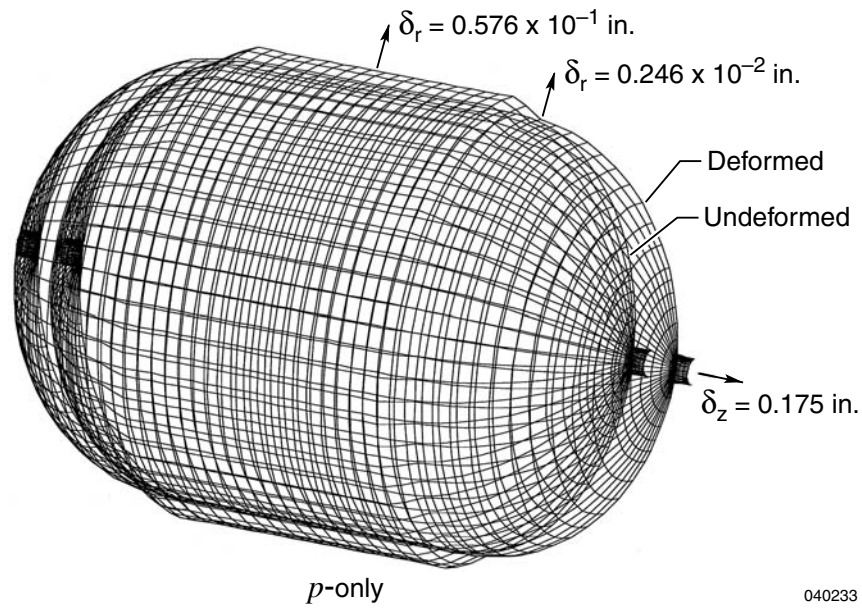
Deformed

Undeformed

$\delta_z = 0.718 \times 10^{-1}$ in.

$p + T$

040232
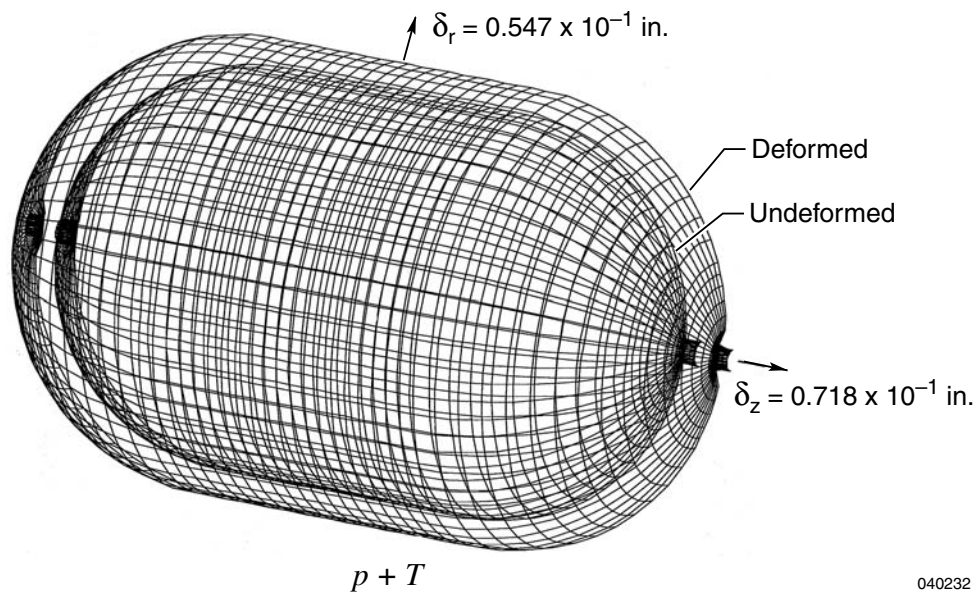
Figure 20. Deformed shape of Helios hemispherical dome tank under internal pressure and temperature loading; $p = 400$ lb/in^2; $T = -120$ °F; hoop-reinforced cylindrical wall.

23

$\delta_r = 0.576 \times 10^{-1}$ in.

$\delta_r = 0.246 \times 10^{-2}$ in.

Deformed

Undeformed

$\delta_z = 0.175$ in.

p-only

040233

Figure 21. Deformed shape of Helios geodesic dome tank under internal pressure loading only; $p = 400$ lb/in^2; hoop-reinforced cylindrical wall.

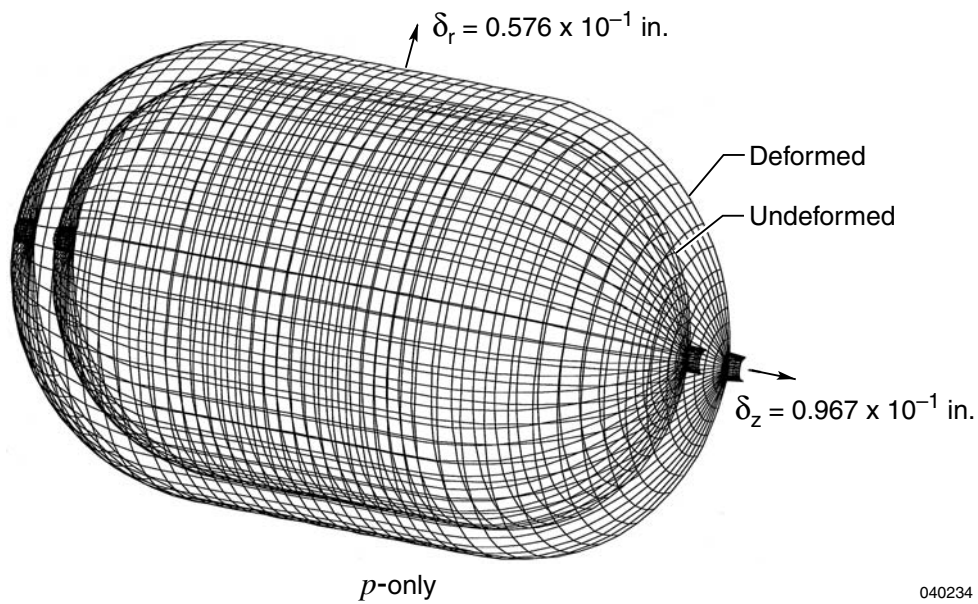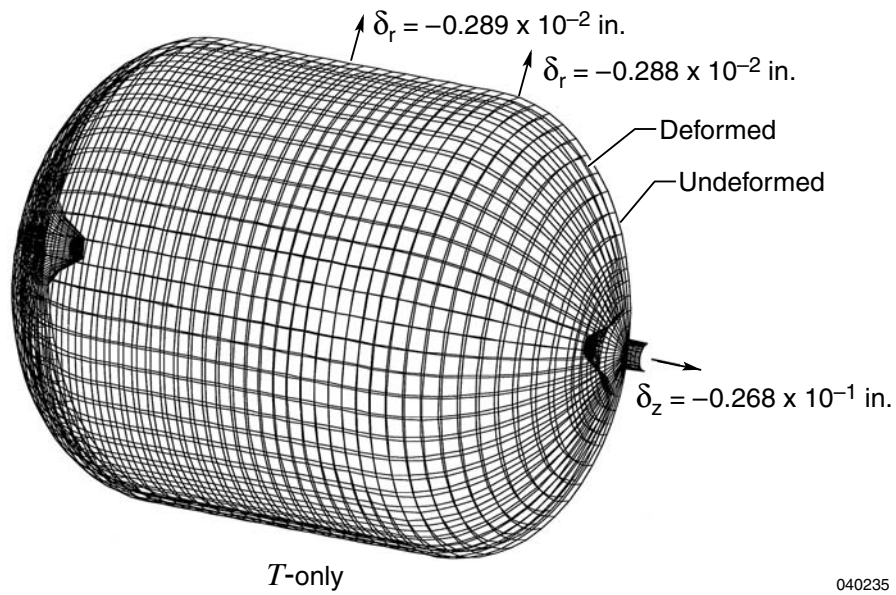$\delta_r = 0.576 \times 10^{-1}$ in.

Deformed

Undeformed

$\delta_z = 0.967 \times 10^{-1}$ in.

p-only

040234

Figure 22. Deformed shape of Helios hemispherical dome tank under internal pressure loading only; $p = 400$ lb/in^2; hoop-reinforced cylindrical wall.

24

$\delta_r = -0.289 \times 10^{-2}$ in.

$\delta_r = -0.288 \times 10^{-2}$ in.

—Deformed

—Undeformed

$\delta_z = -0.268 \times 10^{-1}$ in.

T-only

040235

Figure 23. Deformed shape of Helios geodesic dome tank under temperature loading only; $T = -120\ °F$; hoop-reinforced cylindrical wall.
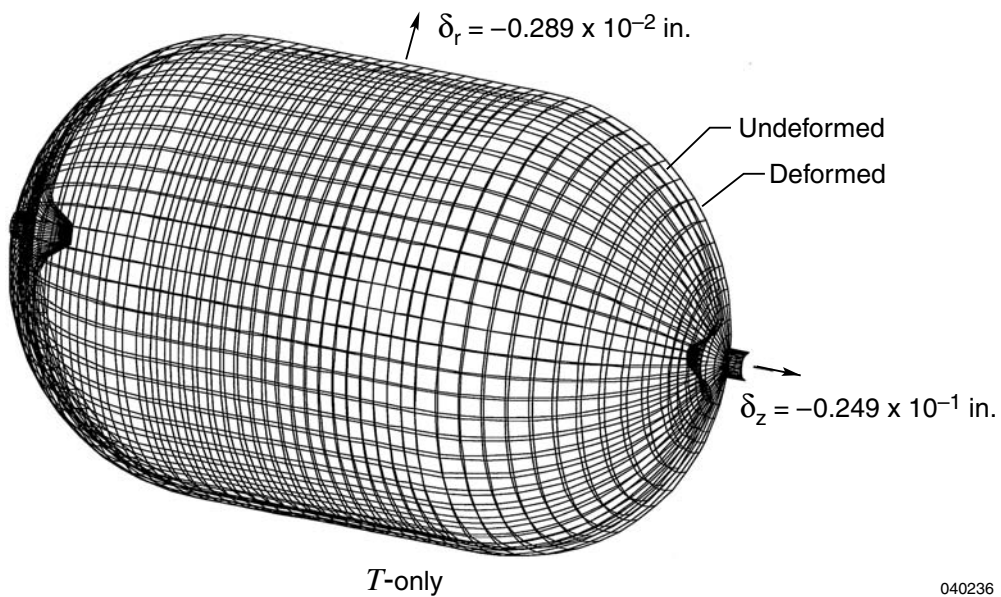

$\delta_r = -0.289 \times 10^{-2}$ in.

—Undeformed

—Deformed

$\delta_z = -0.249 \times 10^{-1}$ in.

T-only

040236

Figure 24. Deformed shape of Helios hemispherical dome tank under temperature loading only; $T = -120\ °F$; hoop-reinforced cylindrical wall.

25
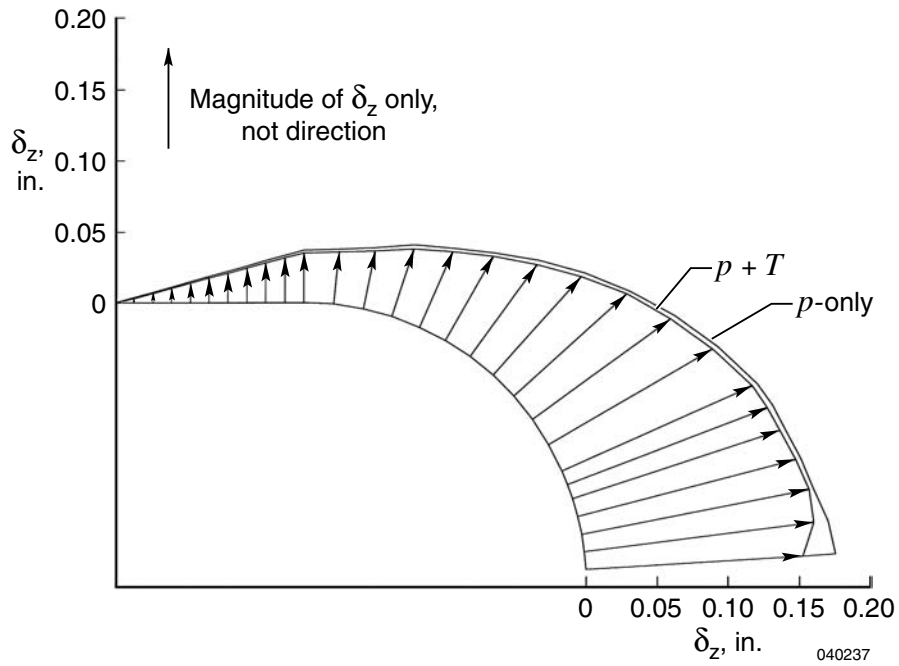
Figure 25. Meridional distributions of axial displacement, δ_z, of Helios geodesic dome tank wall; $p = 400$ lb/in^2; $T = -120$ °F; hoop-reinforced cylindrical wall.
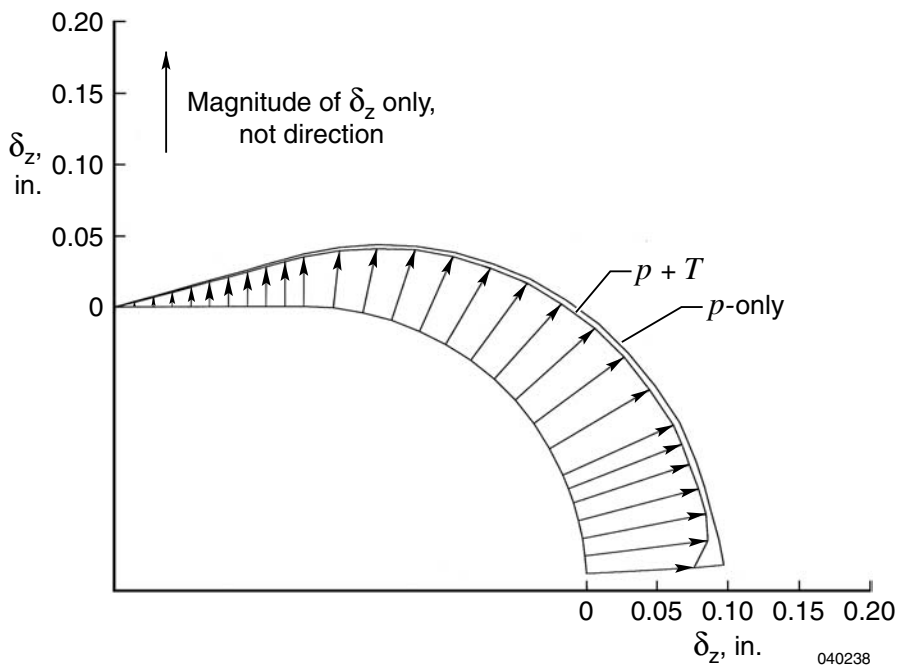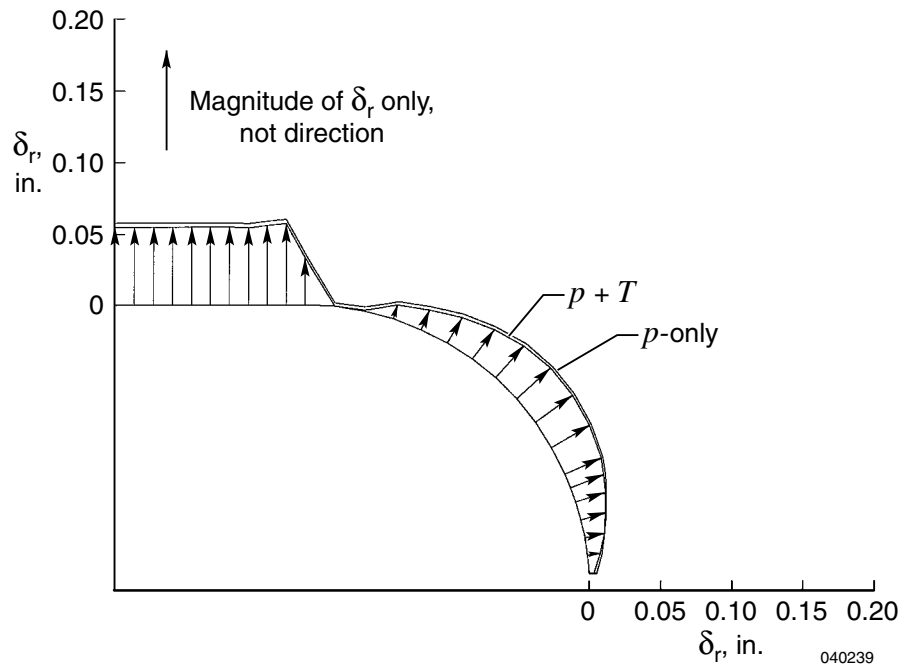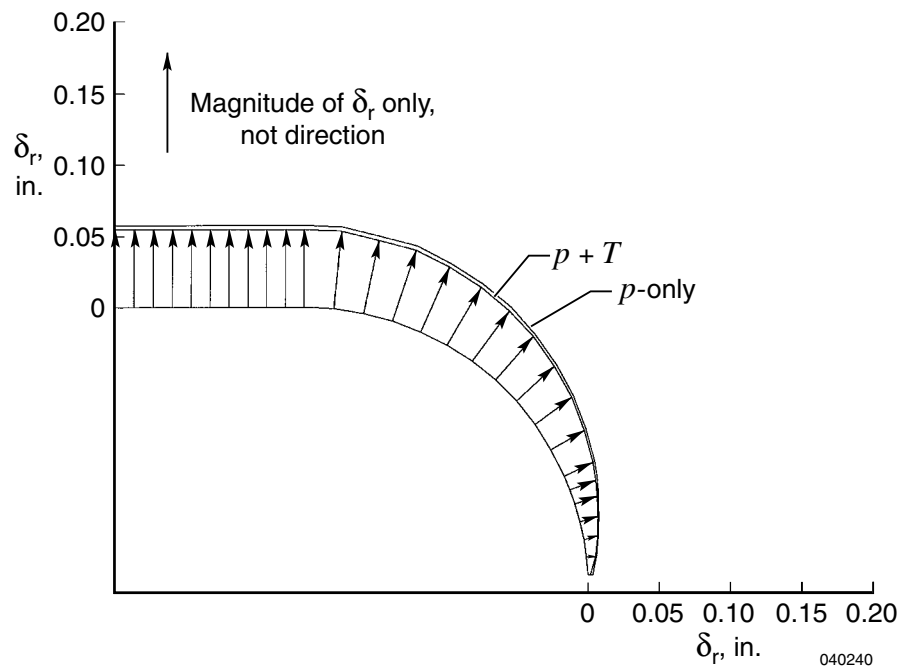

Figure 26. Meridional distributions of axial displacement, δ_z, of Helios hemispherical dome tank wall; $p = 400$ lb/in^2; $T = -120$ °F; hoop-reinforced cylindrical wall.

26

Figure 27. Meridional distributions of radial displacement, δ_r, of Helios geodesic dome tank wall; $p = 400$ lb/in^2; $T = -120$ °F; hoop-reinforced cylindrical wall.

Figure 28. Meridional distributions of radial displacement, δ_r, of Helios hemispherical dome tank wall; $p = 400$ lb/in^2; $T = -120$ °F; hoop-reinforced cylindrical wall.

27
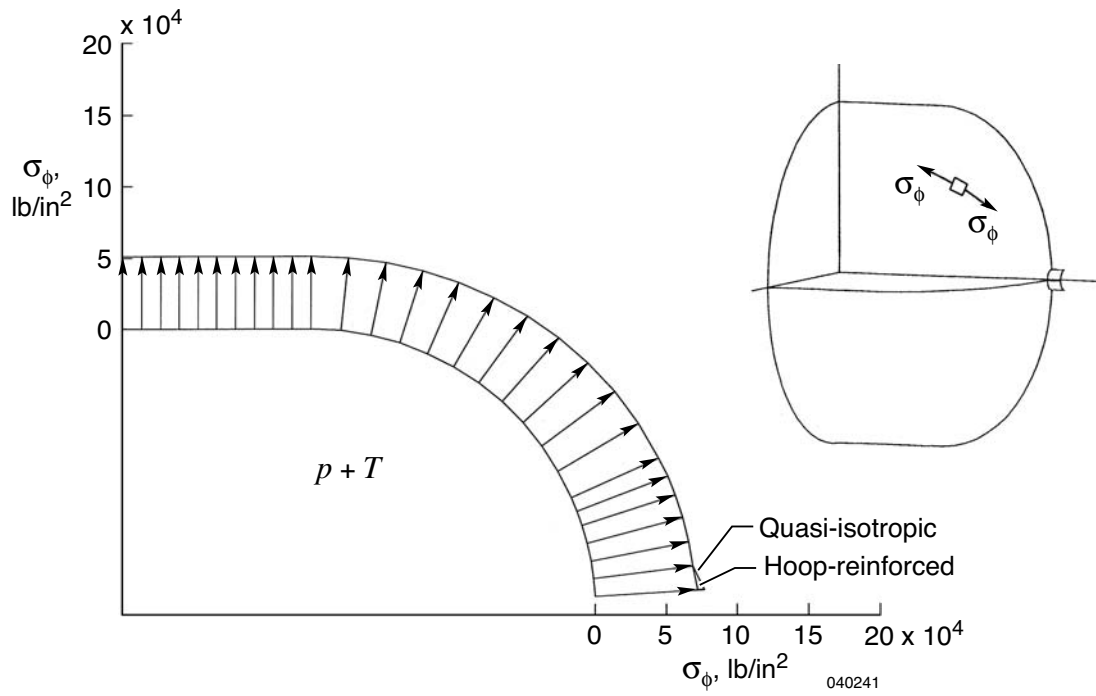
Figure 29. Meridional distributions of meridional stress, σ_ϕ, in Helios geodesic dome tank; $p = 400$ lb/in^2; $T = -120$ °F; hoop-reinforced cylindrical wall.
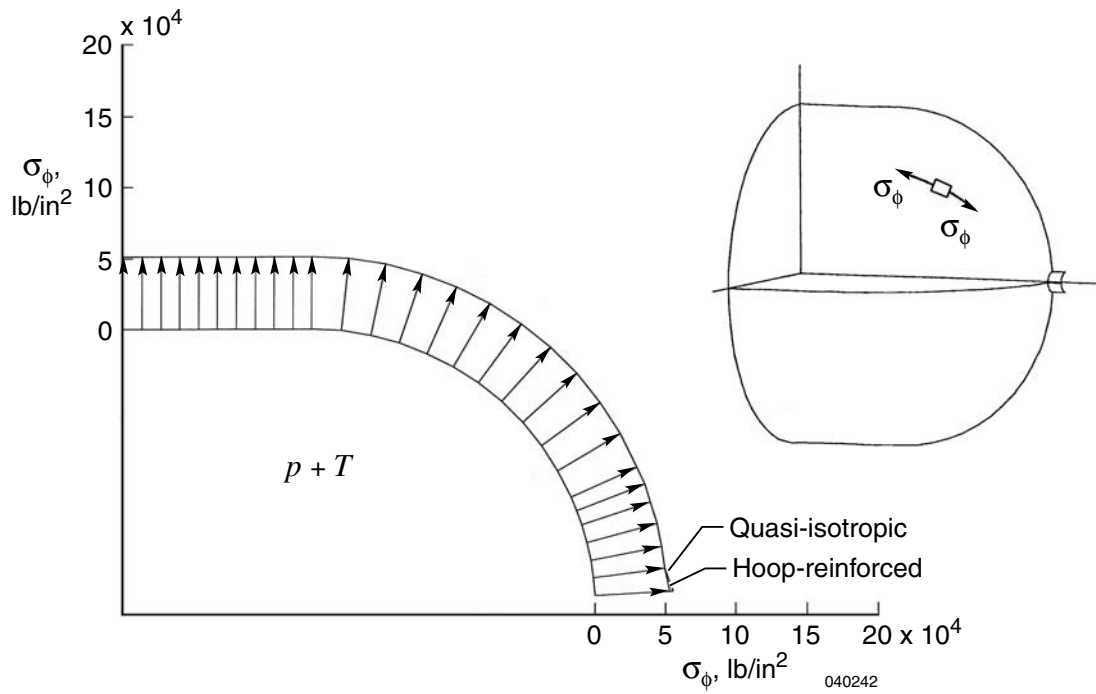

Figure 30. Meridional distributions of meridional stress, σ_ϕ, in Helios hemispherical dome tank; $p = 400$ lb/in^2; $T = -120$ °F; hoop-reinforced cylindrical wall.
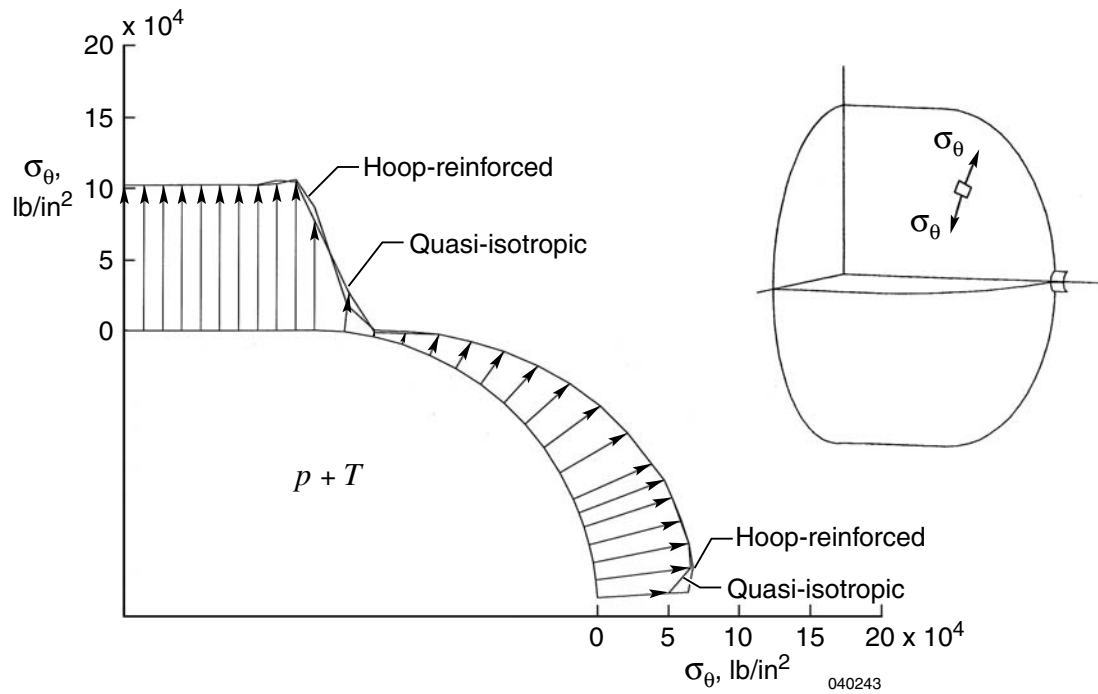
Figure 31. Meridional distributions of hoop stress, σ_θ, in Helios geodesic dome tank; $p = 400$ lb/in^2; $T = -120$ °F; hoop-reinforced cylindrical wall.

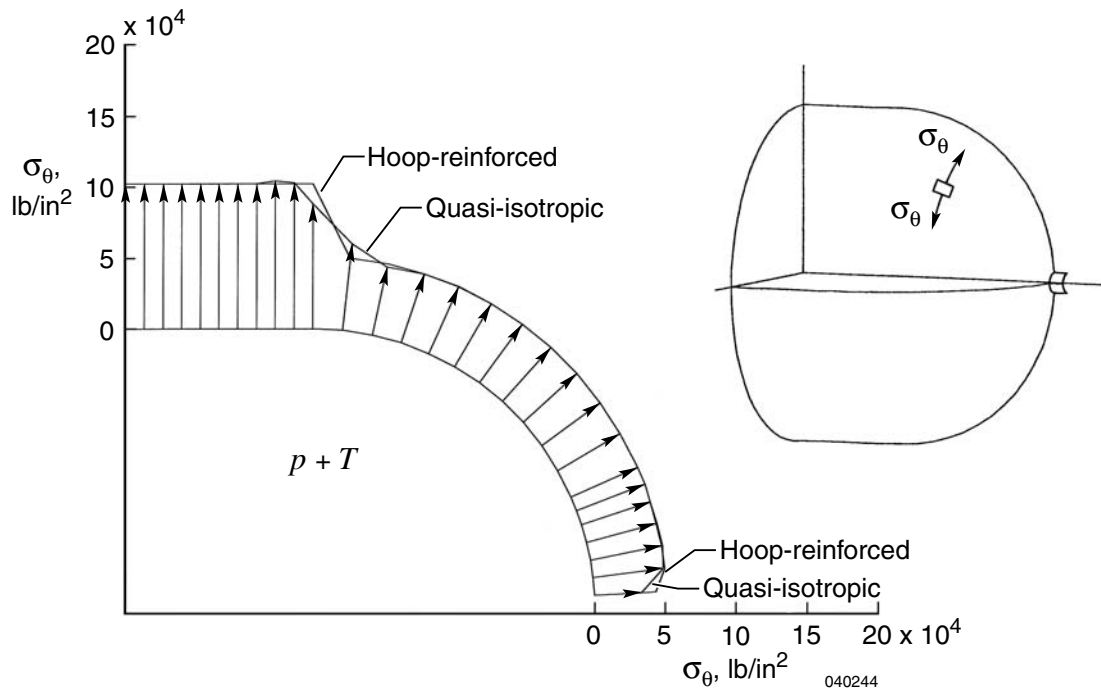
Figure 32. Meridional distributions of hoop stress, σ_θ, in Helios hemispherical dome tank; $p = 400$ lb/in^2; $T = -120$ °F; hoop-reinforced cylindrical wall.

APPENDIX

DEFORMATIONS OF A GEODESIC DOME

This section examines a peculiar structural behavior in which a very small radial displacement occurs at the cylinder-dome juncture of the geodesic dome tank under pressure loading only and combined pressure and temperature loading. For this study, an isolated geodesic dome shell is considered by eliminating the effects of both the cylindrical section and polar boss.

Figure A-1 shows the undeformed and deformed shapes of the geodesic dome under pressure loading only. The radial displacement of $\delta_r = 0.305 \times 10^{-2}$ in. for the isolated geodesic dome is slightly larger than $\delta_r = 0.134 \times 10^{-2}$ in. for the polar boss (fig. 7).

Figure A-2 shows the undeformed and deformed shapes of the geodesic dome under combined pressure and temperature loading. The cooling effect reduced the radial displacement, δ_r, to 0.160×10^{-3} in., which is nearly zero. By contrast, as shown in figures A-3 and A-4, the hemispherical dome does not exhibit this small radial displacement at the cylinder-dome juncture.
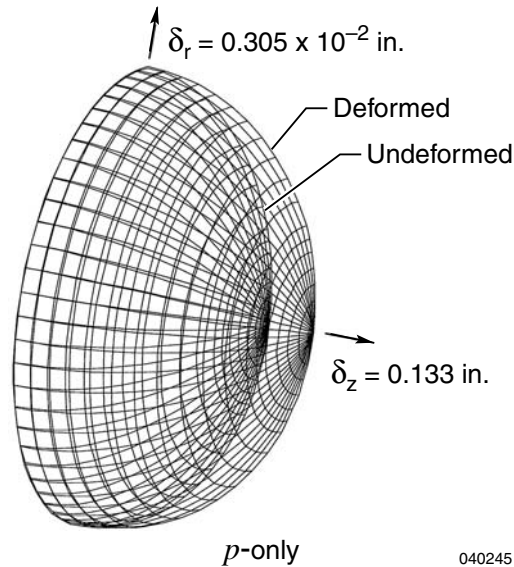

$\delta_r = 0.305 \times 10^{-2}$ in.

Deformed

Undeformed

$\delta_z = 0.133$ in.

p-only   040245

Figure A-1. Deformed shape of geodesic dome shell under internal pressure loading only; $p = 400$ lb/in^2; quasi-isotropic wall.

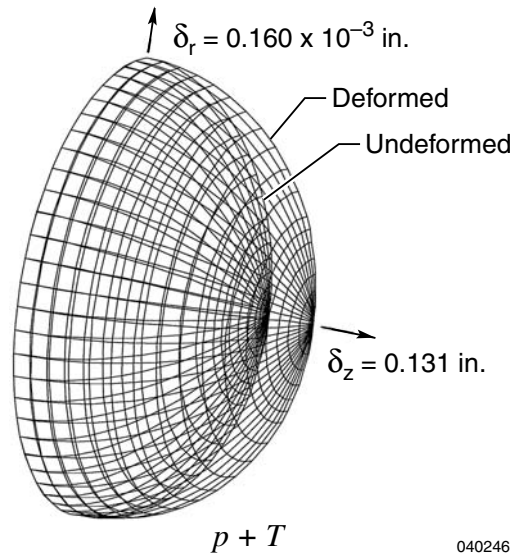$\delta_r = 0.160 \times 10^{-3}$ in.

Deformed

Undeformed

$\delta_z = 0.131$ in.

$p + T$

040246

Figure A-2. Deformed shape of geodesic dome shell under internal pressure and temperature loading; $p = 400$ lb/in^2; $T = -120$ °F; quasi-isotropic wall.

$\delta_r = 0.577 \times 10^{-1}$ in.

Deformed

Undeformed

$\delta_z = 0.592 \times 10^{-1}$ in.

p-only

040446
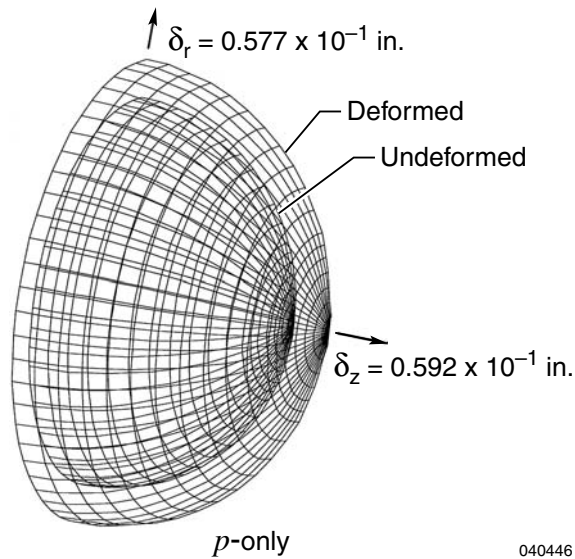
Figure A-3. Deformed shape of hemispherical dome shell under internal pressure loading only; $p = 400$ lb/in^2; quasi-isotropic wall.

$\delta_r = 0.548 \times 10^{-1}$ in.

Deformed

Undeformed

$\delta_z = 0.563 \times 10^{-1}$ in.

$p + T$

040447
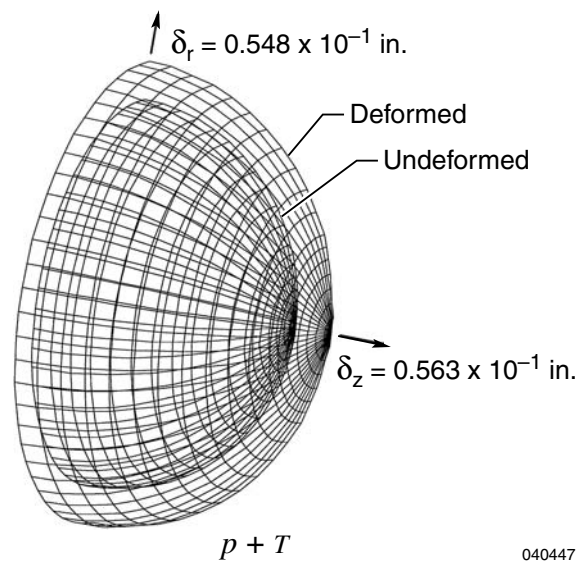
Figure A-4. Deformed shape of hemispherical dome shell under internal pressure and temperature loading; $p = 400$ lb/in^2; $T = -120$ °F; quasi-isotropic wall.

REFERENCES

1. Haddock, R. C., E. E. Morris, and F. J. Darms, Jr., "Safety of Filament Wrapped Graphite/Epoxy Composite Pressure Vessels for Aerospace Applications," AIAA-91-2409, June 1991.

2. Morris, Edgar E., "Advances in Composite Fiber/Metal Pressure Vessel Technology," AIAA-89-2643, July 1989.

3. Morris, E. E., M. Segimoto, and V. Lynn, "Lighter Weight Fiber/Metal Pressure Vessels Using Carbon Overlap," AIAA-86-1504, June 1986.

4. Morris, Edgar E., "Commercial Filament Wound Pressure Vessels for Military and Aerospace Applications," *Aerospace Congress & Exposition*, Anaheim, California, Oct. 5–8, 1981.

5. Radtke, W., H. Krings, R. Forster, J. Klug, and M. Weck, "Manufacturing Techniques for Lightweight Tankage," AIAA-88-2850, July 1988.

6. Braun, C. A., and R. C. Haddock, "Manufacturing Process Controls for High Reliability Carbon Filament-Wound Seamless-Aluminum-Lined Composite Pressure Vessels," AIAA-92-3609, July 1992.

7. Denost, J. P., "New Design Concepts for Filament-Wound Pressure Vessel With Unequal Polar Openings," AIAA-82-1067, June 1982.

8. Hanson, Morgan P., Hadley T. Richards, and Robert O. Hickel, *Preliminary Investigation of Filament-Wound Glass-Reinforced Plastics and Liners for Cryogenic Pressure Vessels*, NASA TN D-2741, March 1965.

9. Riley, Malcolm W., "Filament Wound Reinforced Plastics: State of the Art," Part 1: "What You Can Expect from the Parts," *Materials in Design Engineering*, Report No. 174, Aug. 1960, pp. 127–146.

10. Abraham, Lewis H., *Structural Design of Missiles and Spacecraft*, McGraw-Hill Book Company, Inc., New York, 1962, p. 150.

11. Faupel, Joseph H., *Engineering Design*, John Wiley and Sons, Inc., New York, 1954, p. 312.

12. Darms, F. J., R. E. Landes, J. W. Lambert, M. C. Zethraeus, and R. McCowan, *Computer Program for the Analysis of Filament-Reinforced Metal-Shell Pressure Vessels*, NASA CR-72124, 1966.

13. Hartung, R. F., *Membrane Analysis of Orthotropic Filament-Wound Pressure Vessels*, Technical Report AD-273-306, U.S. Department of Commerce, National Technical Information Service, Feb. 1962.

14. Whetstone, W. D., *SPAR Structural Analysis System Reference Manual*, System Level 13A, vol. 1, Program Execution, NASA CR-158970-1, 1978.

REPORT DOCUMENTATION PAGE		*Form Approved* OMB No. 0704-0188

The public reporting burden for this collection of information is estimated to average 1 hour per response, including the time for reviewing instructions, searching existing data sources, gathering and maintaining the data needed, and completing and reviewing the collection of information. Send comments regarding this burden estimate or any other aspect of this collection of information, including suggestions for reducing this burden, to Department of Defense, Washington Headquarters Services, Directorate for Information Operations and Reports (0704-0188), 1215 Jefferson Davis Highway, Suite 1204, Arlington, VA 22202-4302. Respondents should be aware that notwithstanding any other provision of law, no person shall be subject to any penalty for failing to comply with a collection of information if it does not display a currently valid OMB control number.
PLEASE DO NOT RETURN YOUR FORM TO THE ABOVE ADDRESS.

1. REPORT DATE *(DD-MM-YYYY)* 31-01-2005	2. REPORT TYPE Technical Memorandum	3. DATES COVERED *(From - To)*

4. TITLE AND SUBTITLE Structural Analysis of Helios Filament-Wound Tanks Subjected to Internal Pressure and Cooling	5a. CONTRACT NUMBER
	5b. GRANT NUMBER
	5c. PROGRAM ELEMENT NUMBER
6. AUTHOR(S) William L. Ko	5d. PROJECT NUMBER
	5e. TASK NUMBER
	5f. WORK UNIT NUMBER 710-10-04-SE-29-00-SPU

7. PERFORMING ORGANIZATION NAME(S) AND ADDRESS(ES) NASA Dryden Flight Research Center Edwards, California 93523-0273	8. PERFORMING ORGANIZATION REPORT NUMBER H-2563

9. SPONSORING/MONITORING AGENCY NAME(S) AND ADDRESS(ES) National Aeronautics and Space Administration Washington, DC 20546-0001	10. SPONSORING/MONITOR'S ACRONYM(S) NASA
	11. SPONSORING/MONITORING REPORT NUMBER NASA/TM-2005-212855

12. DISTRIBUTION/AVAILABILITY STATEMENT
Unclassified -- Unlimited
Subject Category 39   Availability: NASA CASI (301) 621-0390

13. SUPPLEMENTARY NOTES
An electronic version can be found at the NASA Dryden Flight Research Center Web site, under Technical Reports.

14. ABSTRACT

A finite-element stress analysis is performed on Helios filament-wound hydrogen tanks to examine the stress field and effect of end dome geometry on the stress field. Each tank is composed of a central circular cylindrical section with either geodesic or hemispherical end domes, which have metallic polar bosses. The tanks are subjected to combined and separate internal pressure and temperature loading conditions, and the stress contributions of each loading component are examined. The tank-wall–polar-boss interfacial meridional tensile stress in the hemispherical dome is found to be approximately 27 percent lower than that in the geodesic dome. The effects of both material anisotropy and the aluminum lining on the intensities of tensile meridional stress at the tank-wall–polar-boss bonding interface are examined.

15. SUBJECT TERMS
Filament-wound tanks, Geodesic dome tank, Hemispherical dome tank, Pressure and temperature loading, Structural performance

16. SECURITY CLASSIFICATION OF:			17. LIMITATION OF ABSTRACT	18. NUMBER OF PAGES	19a. NAME OF RESPONSIBLE PERSON STI Help Desk (email: help@sti.nasa.gov)
a. REPORT	b. ABSTRACT	c. THIS PAGE			19b. TELEPHONE NUMBER *(Include area code)*
U	U	U	UU	40	(301) 621-0390

Standard Form 298 (Rev. 8-98)
Prescribed by ANSI Std. Z39-18